Configuration mixing and intertwined quantum phase transitions in odd-mass niobium isotopes

N. Gavrielov *

Center for Theoretical Physics, Sloane Physics Laboratory, Yale University, New Haven, Connecticut 06520-8120, USA and Racah Institute of Physics, The Hebrew University, Jerusalem 91904, Israel

(Received 16 May 2023; accepted 30 June 2023; published 20 July 2023)

Nuclei in the $Z \approx 40, N \approx 60$ region have one of the most complicated structural evolutions across the nuclear chart, with coexisting shapes arising from different mixed configurations. In such a region, it is difficult to investigate odd-mass nuclei. In this paper a new algebraic framework is introduced: the interacting boson-fermion model with configuration mixing. Using this framework, with a boson core and a proton in the $1f_{5/2}, 2p_{3/2}, 2p_{1/2}, 1g_{9/2}$ orbits, a calculation is carried out to understand the structural evolution of the odd-mass niobium isotopes ($Z = 41$) with neutron number 52–62. The calculated results are compared to energy levels, two-neutron separation energies, $E2$ and $M1$ transition rates, and quadrupole and magnetic moments. The detailed analysis discloses the effects of an abrupt crossing of states between normal and intruder configurations [Type II quantum phase transition (QPT)], which is accompanied by a gradual evolution from spherical- to deformed-core shapes within the intruder configuration (Type I QPT), where both types of QPTs occur around the critical point of neutron number 60. The identification of both types of QPTs in the same chain of isotopes provides an empirical manifestation of intertwined quantum phase transitions (IQPTs) in odd-mass nuclei and the relevance of IQPTs to the niobium chain.

DOI: 10.1103/PhysRevC.108.014320

I. INTRODUCTION

A. Intertwined quantum phase transitions in odd-mass nuclei

Quantum phase transitions (QPTs) [1,2] are structural changes induced by variation of parameters in the Hamiltonian, and are considered pivotal for understanding the dynamics of atomic nuclei [3] and other systems [4].

In nuclear structure, most of the attention has been devoted to the evolution of structure exhibiting two types of phase transitions. The first type of QPT, denoted as Type I [5], is a shape-phase transition in a single configuration. One common approach for investigating Type I QPTs is by using Hamiltonians composed of two (or more) different parts [6]:

$$\hat{H} = (1 - \xi)\hat{H}_1 + \xi\hat{H}_2. \tag{1}$$

In Eq. (1) one examines the equilibrium shape and symmetry of the Hamiltonian, which vary from those of $\hat{H}_1$ to those of $\hat{H}_2$ as the control parameter ξ is varied from 0 to 1. Type I QPTs have been established in the neutron number 90 region for Nd-Sm-Gd-Dy isotopes, where the shape of the nuclei evolves from spherical to deformed [3].

The second type of QPT, denoted as Type II, is a transition in two (or more) configurations that coexist [7] and cross. One common approach for investigating Type II QPTs is by using Hamiltonians composed of a matrix form [8]. For two configurations, this reads

$$\hat{H} = \begin{bmatrix} \hat{H}_{\rm A}(\xi_{\rm A}) & \hat{W}(\omega) \\ \hat{W}(\omega) & \hat{H}_{\rm B}(\xi_{\rm B}) \end{bmatrix}, \tag{2}$$

where $\hat{H}_{\rm A}$ and $\hat{H}_{\rm B}$ denote the A configuration (normal) and B configuration (intruder) Hamiltonians and $\hat{W}$ their coupling. In Eq. (2), one examines the evolution of structure from A to B by varying the control parameters $\xi_{\rm A}$, $\xi_{\rm B}$ and ω. Type II QPTs have been established in nuclei near shell closure, e.g., in the light Pb-Hg isotopes, with strong mixing between the configurations.

A Type II QPT occurs when protons and neutrons that occupy spin-orbit partner orbitals, $\pi(n\ell_{\ell\pm1/2})$–$\nu(n\ell_{\ell\mp1/2})$, interact via the residual isoscalar proton-neutron interaction, V_{pn} [9]. The resulting gain in n-p energy compensates the loss in single-particle and pairing energy. As a consequence, a mutual polarization effect occurs, which lowers single-particle orbitals of higher configurations to near (and effectively below) the ground state configuration. If the mixing is small, the Type II QPT can be accompanied by a distinguished Type I QPT within each configuration separately. Such a scenario, referred to as intertwined QPTs (IQPTs), was recently shown to occur in the even-even zirconium (Zr) isotopes [10–12].

Most studies of QPTs in nuclei have focused on systems with even numbers of protons and neutrons [3,6,7,13,14]. The structure of odd-mass nuclei is more complex due to the simultaneous presence of both collective and single-particle degrees of freedom. Consequently, QPTs in such nuclei have been far less studied. Fully microscopic approaches to QPTs in medium-heavy odd-mass nuclei, such

*noam.gavrielov@yale.edu

as large-scale shell model [15] and beyond-mean-field methods [16], were suggested. However, they are computationally demanding. Other approaches have also been proposed including algebraic frameworks (shell-model inspired [17,18] and symmetry-based [19–26]) and density functionals-based mean-field methods [27–30], involving particle-core coupling schemes with boson-fermion or collective Hamiltonians. So far, these approaches were restricted to Type I QPTs in odd-mass nuclei without configuration mixing.

As mentioned in previous works [29,31–34], there is a growing need to develop a tractable framework that incorporates mixing of multiple configurations in odd-mass nuclei. This task is carried out in the present paper.

B. The niobium isotopes

One region in the nuclear chart that is considered to accommodate mixed configurations and undergo a Type II QPT is the $Z \approx 40$ region near neutron number 60. In this region, the ground state wave function seems to be dominated by a spherical configuration for neutron number 50–58 and by a deformed configuration for neutron number 60 and above [9,35–37].

The sudden onset of deformation has been ascribed in the shell model to V_{pn} between nucleons that occupy the $\pi(1g_{9/2})$–$\nu(1g_{7/2})$ spin-orbit partners [9,36–38], which results in a crossing between the normal and intruder configurations. The crossing arises as the $\nu(2d_{5/2}, 3s_{1/2}, 2d_{3/2}, 1g_{7/2}, 1h_{11/2})$ orbits are filled, which induces a promotion of the protons across the $Z = 40$ subshell gap. This promotion creates 2p-2h intruder excitations [9,39] and the so-called configuration mixing scenario in this region. Promoting the protons also generates a quenching in the difference between the single-particle energies of the $\pi(2p_{1/2})$–$\pi(2p_{3/2})$ orbits [40]. Subsequently, it was also found [41] that alongside the $\pi(2p_{1/2}), \pi(2p_{3/2})$ orbits the $\pi(1f_{5/2})$ orbit contributes significantly to the intruder excitations of the $\pi(1g_{9/2})$ orbit in the lighter ^{92,94,96}Zr isotopes. This contribution was also demonstrated in the recent Monte-Carlo shell model [42] calculation for the chain of the even-even Zr isotopes with neutron number 50–70.

These dramatic structural changes have attracted considerable theoretical and experimental interest (for reviews see [7,43]). For odd-A nuclei, different theoretical approaches have studied this region, including nonrelativistic mean-field based methods [29,32,44–46], shell model approaches [41,47–50], and algebraic approaches [31,33,51–54], where large-scale shell model approaches are scarce [55,56].

The structure of niobium (Nb) isotopes ($Z = 41$) with neutron number 52–62 was recently investigated for first time within the new framework of the interacting boson-fermion model with configuration mixing [57]. The positive-parity states were analyzed to exemplify the occurrence of IQPTs, similarly to the adjacent even-even Zr isotopes [10,12]. In this work, the analysis of Ref. [57] is extended to the negative-parity states, along with more observables that are compared to experimental data. This comparison is further supported by analyzing the configuration and single-particle content of the wave functions for the entire chain.

C. Layout

The paper is divided into the following sections. Section II presents the theoretical framework, which includes the boson Hamiltonian (Sec. II A), fermion Hamiltonian (Sec. II B), boson-fermion interaction (Sec. II C), electromagnetic transitions operators (Sec. II D), and wave functions (Sec. II E). In Sec. III QPTs in the Nb chain are discussed, presenting Type I and Type II QPTs in odd-mass nuclei (Sec. III A) and the Nb model space for the IBFM-CM (Sec. III B).

The results are divided into two main sections. In Sec. IV the results for the individual isotopes are presented, which include spectrum analysis. This section is further partitioned into positive-parity states (Sec. IV A), in the $^{93-97}$Nb region (Sec. IV A 1) and the $^{99-103}$Nb region (Sec. IV A 2), and negative-parity states (Sec. IV B), in the $^{93-97}$Nb region (Sec. IV B 1) and the $^{99-103}$Nb region (Sec. IV B 2). Section V presents results for the evolution of configuration and single-particle content (Sec. V A), energy levels (Sec. V B), two-neutron separation energies (Sec. V C), $E2$ transition rates and quadrupole moments (Sec. V D), and $M1$ and magnetic moments (Sec. V E). The conclusions and outlook are in Sec. VI.

II. THEORETICAL FRAMEWORK

For the study of QPTs in the Nb isotopes the algebraic framework of the interacting boson-fermion model (IBFM) [18] is used. The IBFM treats odd-A nuclei as a system of monopole (s) and quadrupole (d) bosons, representing valence nucleon pairs, and a single (unpaired) nucleon. In a previous paper [57], the IBFM was extended to include core excitations and obtain a boson-fermion model with configuration mixing (IBFM-CM). In such a model, the Hamiltonian has the form

$$\hat{H} = \hat{H}_{\rm b} + \hat{H}_{\rm f} + \hat{V}_{\rm bf}, \tag{3}$$

where $\hat{H}_{\rm b}$ is the boson core Hamiltonian, $\hat{H}_{\rm f}$ is fermion single-particle Hamiltonian, and $\hat{V}_{\rm bf}$ is the boson-fermion interaction.

A. The boson Hamiltonian

For a single configuration, the interacting boson model (IBM) Hamiltonian consists of Hermitian and rotational-scalar interactions that conserve the total number of s and d bosons,

$$\hat{N} = \hat{n}_s + \hat{n}_d = s^\dagger s + \sum_\mu d^\dagger_\mu d_\mu. \tag{4}$$

The latter is fixed by the microscopic interpretation of the IBM [58] to be $N = N_\pi + N_\nu$, where N_π (N_ν) is the number of proton (neutron) particle or hole pairs counted from the nearest closed shell. For multiple shell model configurations, different shell model spaces of 0p-0h, 2p-2h, 4p-4h, ... particle-hole excitations are associated with the corresponding boson spaces of $N, N+2, N+4, \ldots$ bosons, respectively, which are subsequently mixed. The boson Hamiltonian ($\hat{H}_{\rm b}$) is

that of the configuration mixing model (IBM-CM) of [59,60], and has the form [8]

$$\hat{H}_{\rm b} = \begin{bmatrix} \hat{H}_{\rm b}^{\rm A}(\xi^{(\rm A)}) & \hat{W}_{\rm b}(\omega) \\ \hat{W}_{\rm b}(\omega) & \hat{H}_{\rm b}^{\rm B}(\xi^{(\rm B)}) \end{bmatrix}. \tag{5}$$

Here $\hat{H}_{\rm b}^{\rm A}(\xi^{(\rm A)})$ represents the normal A configuration (N boson space) and $\hat{H}_{\rm b}^{\rm B}(\xi^{(\rm B)})$ represents the intruder B configuration ($N+2$ boson space), corresponding to 2p-2h excitations across the (sub)shell closure. Standard forms of $\hat{H}_{\rm b}^{i}(\xi^{i})$ with $i = {\rm A}, {\rm B}$ include pairing, quadrupole, and rotational terms, in the following form [12]:

$$\hat{H}_{\rm b}^{i} = \epsilon_d^{(i)}\hat{n}_d + \kappa^{(i)}\hat{Q}_\chi \cdot \hat{Q}_\chi + \kappa'^{(i)}\hat{L}\cdot\hat{L} + \delta_{i,{\rm B}}\Delta, \tag{6}$$

where Δ is the offset energy between configurations A and B, the quadrupole operator is

$$\hat{Q}_\chi = d^\dagger s + s^\dagger \tilde{d} + \chi(d^\dagger \tilde{d})^{(2)}, \tag{7}$$

and the mixing term is

$$\hat{W}_{\rm b} = \omega[(d^\dagger d^\dagger)^{(0)} + (s^\dagger)^2] + {\rm H.c.}, \tag{8}$$

where H.c. stands for Hermitian conjugate. In Eqs. (7) and (8) $\tilde{d}_\mu = (-)^\mu d_{-\mu}$. Such IBM-CM Hamiltonians have been used extensively for the study of shape coexistence, configuration mixing, and QPTs in even-even nuclei [10–12,59–67].

B. The fermion Hamiltonian

The fermion Hamiltonian ($\hat{H}_{\rm f}$) of Eq. (3) has the form

$$\hat{H}_{\rm f} = \begin{bmatrix} \sum_j \epsilon_j^{(\rm A)}\hat{n}_j & 0 \\ 0 & \sum_j \epsilon_j^{(\rm B)}\hat{n}_j \end{bmatrix}, \tag{9}$$

where j is the angular momentum of the occupied orbit, $\hat{n}_j = \sum_\mu a_{j\mu}^\dagger a_{j\mu}$ the corresponding number operator and $\epsilon_j^{(\rm i)}$ ($i = {\rm A}, {\rm B}$) are the single-particle energies for each configuration, A or B. In this work, the single-particle energies are determined using the microscopic interpretation of the IBFM [18] (see the Appendix for more details).

C. The boson-fermion interaction

The boson-fermion interaction has the form

$$\hat{V}_{\rm bf} = \begin{bmatrix} \hat{V}_{\rm bf}^{\rm A}(\zeta^{(\rm A)}) & \hat{W}_{\rm bf}(\omega_j) \\ \hat{W}_{\rm bf}(\omega_j) & \hat{V}_{\rm bf}^{\rm B}(\zeta^{(\rm B)}) \end{bmatrix}. \tag{10}$$

Here, $\hat{V}_{\rm bf}^{(i)}$ ($i = {\rm A}, {\rm B}$) is the general boson-fermion interaction [18] for each configuration. In this work it involves monopole, quadrupole, and exchange terms

$$\hat{V}_{\rm bf}^{(i)} = V_{\rm bf}^{{\rm MON}(i)} + V_{\rm bf}^{{\rm QUAD}(i)} + V_{\rm bf}^{{\rm EXC}(i)}, \tag{11}$$

which read

$$V_{\rm bf}^{{\rm MON}(i)} = \sum_j A_j^{(i)}[[d^\dagger \times \tilde{d}]^{(0)} \times [a_j^\dagger \times \tilde{a}_j]^{(0)}]_0^{(0)}, \tag{12a}$$

$$V_{\rm bf}^{{\rm QUAD}(i)} = \sum_{jj'} \Gamma_{jj'}^{(i)}[\hat{Q}_\chi \cdot [a_j^\dagger \times \tilde{a}_{j'}]^{(2)}]_0^{(0)}, \tag{12b}$$

$$V_{\rm bf}^{{\rm EXC}(i)} = \sum_{jj'j''} \Lambda_{jj'}^{j''(i)} : [[d^\dagger \times \tilde{a}_j]^{(j'')} \times [\tilde{d} \times a_{j'}^\dagger]^{(j'')}]_0^{(0)} :, \tag{12c}$$

where $\tilde{a}_{j\mu} = (-)^{j+\mu}a_{j-\mu}$. Using the microscopic interpretation of the IBFM [18], these couplings can be expressed in terms of strengths ($A_0^{(i)}$, $\Gamma_0^{(i)}$, $\Lambda_0^{(i)}$) and occupation probabilities (u_j, v_j) (see the Appendix for more details). The new off-diagonal term contributes to the j-dependent mixing

$$\hat{W}_{\rm bf}(\omega_j) = \sum_j \omega_j \hat{n}_j[(d^\dagger d^\dagger)^{(0)} + (s^\dagger)^2 + {\rm H.c.}]. \tag{13}$$

D. Electromagnetic transitions operators

Operators inducing electromagnetic transitions of type σ and multipolarity L contain boson and fermion parts,

$$\hat{T}(\sigma L) = \hat{T}_{\rm b}(\sigma L) + \hat{T}_{\rm f}(\sigma L). \tag{14}$$

For $\sigma L = E2$ transitions, the boson and fermion parts of Eq. (14) are

$$\hat{T}_{\rm b}(E2) = e^{(\rm A)}\hat{Q}_\chi^{(N)} + e^{(\rm B)}\hat{Q}_\chi^{(N+2)}, \tag{15a}$$

$$\hat{T}_{\rm f}(E2) = \sum_{jj'} f_{jj'}^{(2)}[a_j^\dagger \times \tilde{a}_{j'}]^{(2)}, \tag{15b}$$

In Eq. (15a), $e^{(\rm A)}$, $e^{(\rm B)}$ are the boson effective charges for configuration A and B, respectively. The superscript (N) denotes a projection onto the $[N]$ boson space, and in Eq. (15b) $f_{jj'}^{(2)}$ reads

$$f_{jj'}^{(2)} = -\frac{e_f}{\sqrt{5}}\langle j||Y_{lm}^{(2)}||j'\rangle, \tag{16}$$

where e_f is the effective charge for $E2$ transitions.

For $\sigma L = M1$ transitions, the boson and fermion parts of Eq. (14) are

$$\hat{T}_{\rm b}(M1) = \sum_i \sqrt{\frac{3}{4\pi}} g^{(i)}\hat{L}^{(N_i)} + \tilde{g}^{(i)}\big[\hat{Q}_\chi^{(N_i)} \times \hat{L}^{(N_i)}\big]^{(1)}. \tag{17a}$$

$$\hat{T}_{\rm f}(M1) = \sum_{jj'} f_{jj'}^{(1)}[a_j^\dagger \times \tilde{a}_{j'}]^{(1)}, \tag{17b}$$

with

$$f_{jj'}^{(1)} = -\frac{f_1}{\sqrt{3}}\langle j||g_l\hat{l} + g_s\hat{s}||j'\rangle. \tag{18}$$

Here, $i = ({\rm A}, {\rm B})$ and $N_{\rm A} = N$, $N_{\rm B} = N+2$. For a proton, the free value for the spin g factor is $g_s = 5.5857\,\mu_N$, and for the angular g factor it is $g_l = 1\,\mu_N$ (see the Appendix for more details about the quenching of g_s).

E. Wave functions

The Hamiltonian of Eq. (3) is diagonalized numerically. The resulting eigenstates, $|\Psi; J\rangle$, are linear combinations of wave functions $\Psi_{\rm A}$ and $\Psi_{\rm B}$, involving bosonic basis states in the two spaces $|[N], \alpha, L\rangle$ and $|[N+2], \alpha, L\rangle$, where α denotes additional quantum numbers characterizing the boson basis used. The boson (L) and fermion (j) angular momenta are coupled to J and the combined wave function has the form

$$|\Psi; J\rangle = \sum_{\alpha,L,j} C_{\alpha,L,j}^{(N,J)}|\Psi_{\rm A}; [N], \alpha, L, j; J\rangle + \sum_{\alpha,L,j} C_{\alpha,L,j}^{(N+2,J)}|\Psi_{\rm B}; [N+2], \alpha, L, j; J\rangle. \tag{19}$$

For such a wave function, it is possible to examine the probability of normal-intruder mixing,

$$P^{(N_i,J)} = \sum_j P_j^{(N_i,J)}, \tag{20}$$

with $P^{(N_A,J)} + P^{(N_B,J)} = 1$. Here, $P_j^{(N_i,J)}$ is the probability of a single-particle orbit j within a certain configuration i:

$$P_j^{(N_i,J)} = \sum_{\alpha,L} \left|C_{\alpha,L,j}^{(N_i,J)}\right|^2. \tag{21}$$

III. QPTs IN THE NIOBIUM CHAIN

A. Type I and Type II QPTs

The occurrence of QPTs in Bose-Fermi systems for a single-configuration in the framework of the IBFM is more complicated than in the case of boson systems (IBM) [24]. QPTs in odd-mass nuclei consider the effect of the odd nucleon on the phase transitions of the boson core. Considering the U(5)-SU(3) boson QPT (Type I), in the adjacent odd-mass system the transition is from a weak coupling [spherical U(5) boson core] to a strong coupling [axially deformed SU(3) boson core] spectrum.

A U(5) spherical spectrum is typically identified with couplings of the fermion orbits j with states L of the adjacent even-even system to give a total angular momentum $J = L \otimes j$,

$$|L - j| \leqslant J \leqslant |L + j|. \tag{22}$$

For the ground state 0^+ of the adjacent even-even isotope, this results in states with a total $J = j$, while for a first-excited 2^+ it results in a multiplet of states, for each of the j orbits. Their respective irreducible representations (irreps) in the boson U(5) limit are $n_d = 0$ and 1. For a single-j coupling, $L \otimes j$, one can compare the energy of the state L of the adjacent even-even nuclei to the "center of gravity" (CoG) [68] of a multiplet of states Eq. (22) by calculating

$$\Delta E_{\mathrm{CoG}} = \frac{\sum_J (2J+1)E_J}{(2L+1)(2j+1)}, \tag{23}$$

where E_J are the excitation energies of the states with total J that belong to the multiplet. The $E2$ [$M1$] transitions between members of the weakly deformed multiplet (originating from the 2^+ with $n_d = 1$) and the single state (originating from the 0^+ with $n_d = 0$) are comparable to [weaker than] those of the adjacent even-even isotope while $E2$ [$M1$] transitions between the multiplet members are weak [strong].

An SU(3) deformed spectrum is typically identified with rotational bands starting at some value K of angular momentum. For a single-j scenario (ignoring K bands mixing), the energy typically behaves as

$$E_K(J) = BJ(J+1), \tag{24}$$

where B is the moment of inertia. The magnetic and quadrupole moments for each of the states in the band and the $M1$ and $E2$ transitions among them can be compared to the geometric collective model expressions of Bohr and Mottelson (BM) [69] for $K \neq 1/2$:

$$Q(J,K) = Q_0 \langle J, K, 2, 0|J, K\rangle \langle J, J, 2, 0|J, J\rangle, \tag{25a}$$

$$\mu(J,K) = g_R J + (g_K - g_R)\frac{K^2}{J+1}, \tag{25b}$$

and

$$B(E2; J', K \to J, K) = Q_0^2 \left(\frac{5}{16\pi}\right) \times \langle J', K, 2, 0|J, K\rangle^2, \tag{26a}$$

$$B(M1; J', K \to J, K) = \frac{3}{4\pi}(g_K - g_R)^2 K^2 \times \langle J', K, 1, 0|J, K\rangle^2, \tag{26b}$$

where Q_0, g_R, and g_K are fitted to the data, and g_R is expected to behave as $g_R \approx Z/A$.

For multiple configurations, one would expect, as in the adjacent even-even case, to observe a crossing of states that are associated with the different configurations that are mixed (Type II QPT), where in a weak mixing scenario the above considerations for transitions would apply for each configuration separately.

B. Niobium model space for IBFM-CM

The ${}^{A}_{41}$Nb isotopes with mass number $A = 93$–103 are described by coupling a proton to their respective ${}_{40}$Zr cores with neutron number 52–62. The latter isotopes have been suggested to have [10–12] a normal A configuration that corresponds to having no active protons above the $Z = 40$ subshell gap, and an intruder B configuration that corresponds to two-proton excitation from below to above this gap, creating 2p-2h states. The parameters of $\hat{H}_{\mathrm{b}}$ (5) and boson numbers are taken to be the same as in a previous calculation of these Zr isotopes. According to the usual boson counting, the corresponding bosonic configurations have

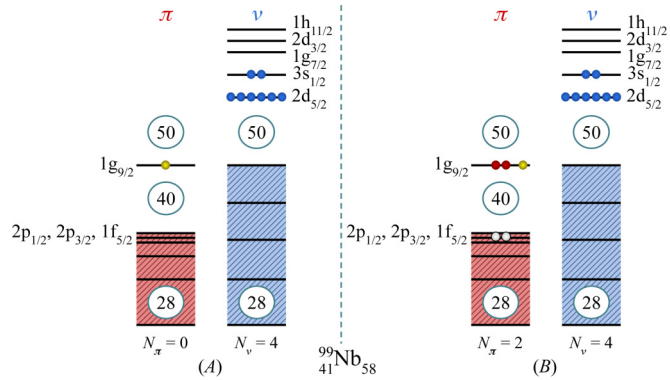

FIG. 1. Schematic representation of the two coexisting shell-model configurations (A and B) for ${}^{99}_{41}$Nb$_{58}$. The corresponding numbers of proton bosons (N_π) and neutron bosons (N_ν), relevant to the IBM-CM, are listed for each configuration and are depicted by a pair of particles (in red or blue) and a pair of holes (in white). There are no active proton bosons for configuration A. Alongside them, the extra proton (in yellow) is shown at the proton $\pi(1g_{9/2})$ orbit.

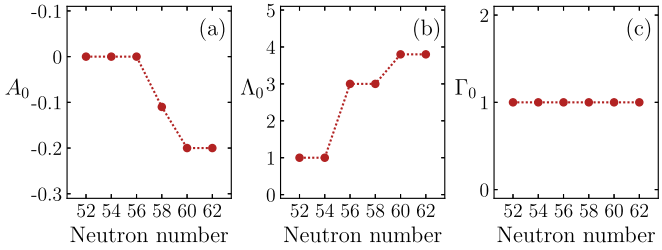

FIG. 2. Parameters of the IBFM-CM boson-fermion interaction, Eq. (11), in MeV. For more details see the Appendix.

proton bosons $N_\pi = 0$ for configuration A and $N_\pi = 2$ for configuration B. Both configurations have neutron bosons $N_\nu = 1, 2, \ldots, 6$ for neutron number 52–62, which sums to a total of $N = 1, 2, \ldots 6$, for $^{92-102}$Zr, respectively (see Table V of [12] for more details). For the odd particle, the valence protons are assumed to reside in the $Z = 28$–50 shell with the $\pi(1f_{5/2}), \pi(2p_{3/2}), \pi(2p_{1/2}), \pi(1g_{9/2})$ orbits. The two configurations and the odd proton are shown schematically in Fig. 1 for ^{99}Nb.

IV. RESULTS: DETAILED QUANTUM ANALYSIS OF INDIVIDUAL ISOTOPES

The quantum analysis for $^{93-103}$Nb entails a detailed comparison of the experimental energies and $E2$ and $M1$ transition rates with the results of the calculation for the positive- and negative-parity states. The strengths of the boson-fermion interaction and single quasiparticle energies take the same value for both configurations, i.e., $A_0^{(i)}, \Gamma_0^{(i)}, \Lambda_0^{(i)} = A_0, \Gamma_0, \Lambda_0$ and $\epsilon_j^{(i)} = \epsilon_j$ for $i =$ A,B, and are shown in Fig. 2 and Tables I and II. The BCS calculation and fitting procedure employed to obtain them are discussed in the Appendix.

The wave functions obtained are of the form of Eq. (19) with $j = \pi(1g_{9/2})$ for the positive-parity sector and $j = \pi(2p_{1/2}), \pi(2p_{3/2}), \pi(1f_{5/2})$ for the negative-parity sector. The negative- and positive-parity calculations are done independently, where the ground state is always positive parity. Therefore, a shift in energy is added to the excitations of the negative-parity energies that places the lowest calculated energy at the experimental value. In Figs. 3–12, and 14 states in black (blue) belong to the normal (intruder) A (B) configuration.

TABLE I. Empirical single-particle energies (E_j) taken from Table XI of [83] and calculated single-quasiparticle energies (ϵ_j) in MeV with occupation probabilities (v_j^2) for the different j orbits, with a resulting Fermi energy of $\lambda_F = 2.024$ MeV.

Orbit	E_j	ϵ_j	v_j^2
$1g_{9/2}$	2.684	1.639	0.299
$2p_{1/2}$	1.753	1.524	0.589
$2p_{3/2}$	0.486	2.148	0.858
$1f_{5/2}$	0.000	2.519	0.902

TABLE II. Parameters in MeV of the boson-fermion interactions, $\hat{V}_{\rm bf}^{(i)}$ of Eq. (11), obtained from a fit assuming $A_0^{(i)} = A_0$, $\Gamma_0^{(i)} = \Gamma_0$, and $\Lambda_0^{(i)} = \Lambda_0$, where ($i =$ A, B).

Neutron number	52	54	56	58	60	62
A_0	0	0	0	−0.11	−0.2	−0.2
Γ_0	1.0	1.0	1.0	1.0	1.0	1.0
Λ_0	1.0	1.0	3.0	3.0	3.8	3.8

A. Positive-parity states

For the positive parity states only the $\pi(1g_{9/2})$ orbit plays a role, which reduces the calculation to a single-j one. The individual isotopes are divided into two regions: a weak coupling region for $^{93-97}$Nb and the IQPT region for $^{99-103}$Nb, which also incorporates strong coupling.

For the region of $^{93-97}$Nb, the calculation is compared to the experimental levels in Figs. 3–5, including $E2$ and $M1$ transitions among them. For each isotope, the spectrum exhibits coexistence of two spherical configurations with weak mixing between them. The corresponding spectra of ^{92,94,96}Zr, the even-even cores, are also shown with an assignment of selected levels L to the normal A or intruder B configurations (in subscript), based on the analysis in Ref. [12], which also showed that the two configurations in ^{92,94,96}Zr are spherical and weakly deformed, respectively.

For the $^{99-103}$Nb region, the calculation is compared to the experimental levels in Figs. 6–8, including $E2$ and $M1$ transitions among them. For ^{99}Nb, the spectrum exhibits coexistence of two configurations, one spherical and one weakly deformed, where only the ground state seems to belong to the normal A configuration. For ^{101,103}Nb, the spectrum exhibits a rotational pattern that resembles a strong coupling scenario within the intruder B configuration.

1. The $^{93-97}$Nb region: Weak coupling

For $^{93-97}$Nb, shown in Figs. 3–5, the weak coupling between the ground state, $0^+_{1;\rm A}$, of $^{92-96}$Zr and the $\pi(1g_{9/2})$ yields the ground state $9/2^+_1$ of $^{93-97}$Nb. For the $2^+_{1;\rm A}$, the coupling to the $\pi(1g_{9/2})$ yields a quintuplet of states. For ^{93}Nb, the experimental states $7/2^+_1(0.744)$, $5/2^+_1(0.809)$, $11/2^+_1(0.979)$, $13/2^+_1(0.950)$, $9/2^+_3(1.297)$ (in parentheses are energies in MeV), are the members of this quintuplet. They have a CoG (23) of 0.976 MeV, which is close to the observed energy 0.935 MeV of the 2^+_1 in ^{92}Zr. For ^{95}Nb, the experimental states $7/2^+_1(0.724)$, $5/2^+_1(0.73)$, $13/2^+_1(0.825)$, $5/2^+$–$13/2^+(1.149)$, $9/2^+_4(1.337)$ are members of this quintuplet. They have a CoG (23) of 0.9776 MeV, which is close to the observed energy 0.919 MeV of the 2^+_1 in ^{94}Zr. For both ^{93,95}Nb the calculation reproduces the energies of the quintuplet to a good degree. For ^{97}Nb there are not enough data to clearly assign the existing states to a given configuration, and this remains to be explored.

The $E2$ transitions from the quintuplet states to the ground state are comparable in magnitude to the $2^+_{1;\rm A} \to 0^+_{1;\rm A}$ transition in $^{92-96}$Zr [6.4(6), 4.9(3), 2.3(3) W.u., respectively]. For ^{93}Nb, the calculation reproduces the data to a good degree,

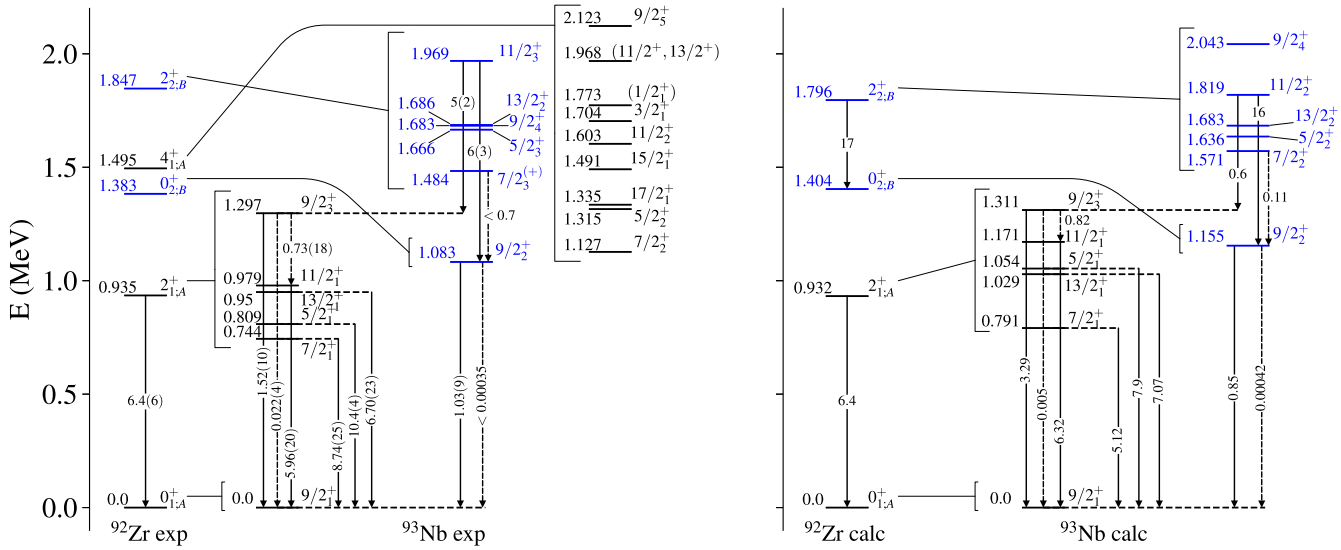

FIG. 3. Experimental (left) and calculated (right) energy levels in MeV, and $E2$ (solid arrows) and $M1$ (dashed arrows) transition rates in W.u., for ^{93}Nb and ^{92}Zr. Normal (intruder) states are depicted in black (blue). Lines connecting L-levels in ^{92}Zr to sets of J-levels in ^{93}Nb indicate the weak coupling $(L \otimes \frac{9}{2})J$. Data taken from [50,70]. Note that the observed $4^+_{1;A}$ state in ^{92}Zr is outside the boson $N = 1$ model space.

except for $9/2^+_3$, whose experimental decay [1.52(10) W.u.] is weaker than the others and the calculation (3.29). For $^{95-97}$Nb there are no measured $E2$ or $M1$ transitions. The $M1$ transitions of ^{93}Nb from the quintuplet to the ground state are weak, the $7/2^+_1 \to 9/2^+_1$, $11/2^+_1 \to 9/2^+_1$, have $B(M1)$ of 0.099(8), 0.085(6) W.u., while $M1$ transitions within states of the quintuplet are strong, the $5/2^+_1 \to 7/2^+_1$, $9/2^+_3 \to 11/2^+_1$, $9/2^+_3 \to 7/2^+_1$ have $B(M1)$ of 0.160(12), 0.73(18), 0.16(3) W.u., as expected for weak coupling to a spherical vibrator [18] and which the calculation suggests. The situation for calculated $E2$ and $M1$ transitions is similar in $^{95-97}$Nb.

In Fig. 3, one can also identify a nonuplet of states, from $(1/2^+_1)$ to $17/2^+_1$, built on the $4^+_{1;A}$ state of ^{92}Zr in the empirical spectrum of ^{93}Nb, with a CoG of 1.591 MeV, close to the 1.495 MeV of $4^+_{1;A}$. This $4^+_{1;A}$ is outside the calculated ^{92}Zr model space (with boson number $N_b = 1$ for the normal A configuration; see [12] for more details) and as a consequence so are the resulting states of ^{93}Nb. Nevertheless, it supports the weak coupling scenario. In Fig. 4, one can also identify

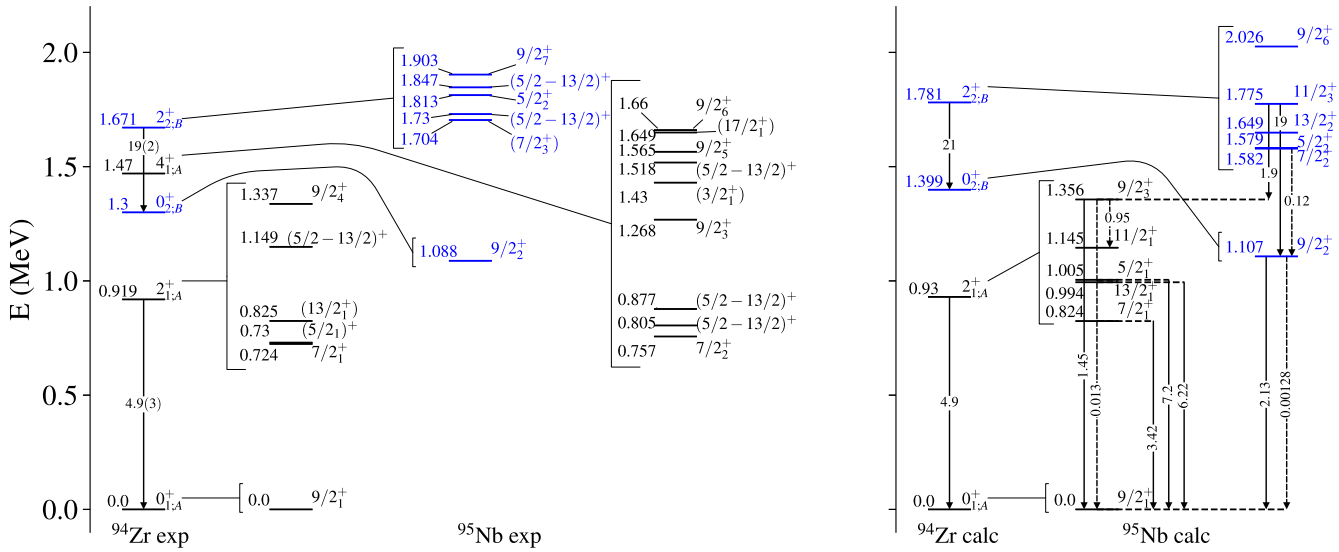

FIG. 4. Experimental (left) and calculated (right) energy levels in MeV, and $E2$ (solid arrows) and $M1$ (dashed arrows) transition rates in W.u., for ^{95}Nb and ^{94}Zr. Normal (intruder) states are depicted in black (blue). Lines connecting L-levels in ^{94}Zr to sets of J-levels in ^{95}Nb indicate the weak coupling $(L \otimes \frac{9}{2})J$. Data taken from [71]. Note that the observed $4^+_{1;A}$ state in ^{94}Zr is considered outside the boson $N = 2$ model space.

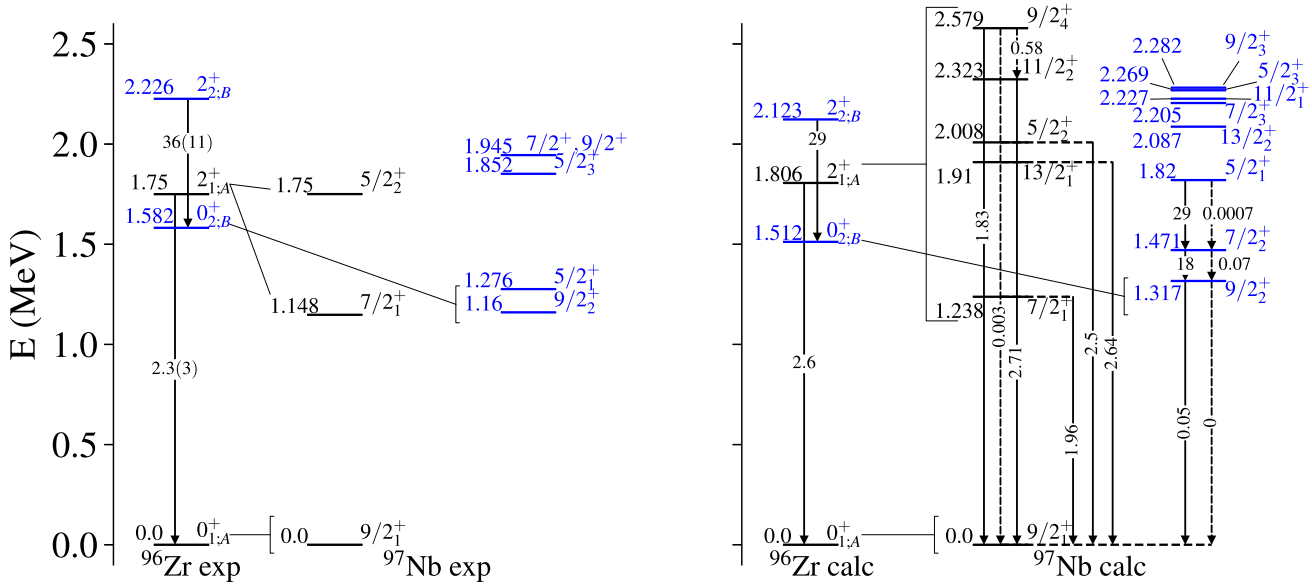

FIG. 5. Experimental (left) and calculated (right) energy levels in MeV, and $E2$ (solid arrows) and $M1$ (dashed arrows) transition rates in W.u., for ^{97}Nb and ^{96}Zr. Normal (intruder) states are depicted in black (blue). Lines connecting L-levels in ^{96}Zr to sets of J-levels in ^{97}Nb indicate the weak coupling $(L \otimes \frac{9}{2})J$. Data taken from [72].

a nonuplet of states, built on the $4^+_{1;A}$ state of ^{94}Zr in the experimental spectrum of ^{95}Nb; however, data to identify all of them and calculate their CoG are lacking.

The IBFM-CM also allows one to identify and analyze the *intruder B configuration* of $^{93-97}$Nb, where the weak coupling scenario is also valid. As shown in Figs. 3–5, the coupling of $\pi(1g_{9/2})$ to the $0^+_{2;B}$ state in $^{92-96}$Zr, yields the excited $9/2^+_2$ state in $^{93-97}$Nb. For the $2^+_{2;B}$ state the coupling yields another quintuplet of states. For ^{93}Nb, it is the experimental $7/2^+_3(1.484)$, $5/2^+_3(1.666)$, $9/2^+_4(1.683)$, $13/2^+_2(1.686)$, $11/2^+_3(1.969)$ that are reproduced to a good degree by the calculation and whose experimental CoG is 1.719 MeV, a bit lower than the energy 1.847 MeV of the $2^+_{2;B}$ of ^{92}Zr. For ^{95}Nb, it is the $7/2^+_3(1.704)$, $(5/2–13/2)^+(1.686)$, $5/2^+_2(1.813)$, $(5/2^+–13/2)^+(1.969)$, $9/2^+_4(1.903)$ that are reproduced to a good degree by the calculation and whose experimental CoG is 1.803 MeV, a bit higher than the energy 1.671 MeV of the $2^+_{2;B}$ of ^{94}Zr. It is interesting to note that the energy difference from the $0^+_{2;B}$, and the $9/2^+_2$ that is associated with it, $E(0^+_{2;B}) - E(9/2^+_2)$, becomes larger when going from ^{93,95}Nb

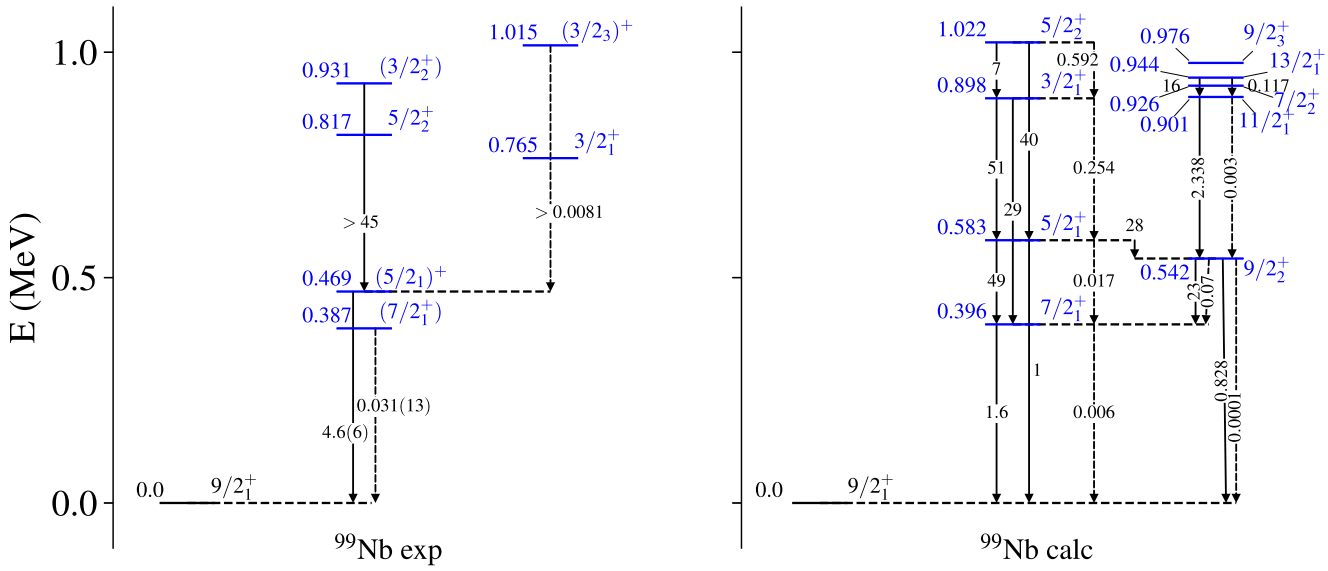

FIG. 6. Experimental (left) and calculated (right) energy levels in MeV, and $E2$ (solid arrows) and $M1$ (dashed arrows) transition rates in W.u., for ^{99}Nb. The $9/2^+_1$ state is assigned to the normal A configuration (depicted in black) and the rest of the states to the intruder B configuration (depicted in blue). Data taken from [73].

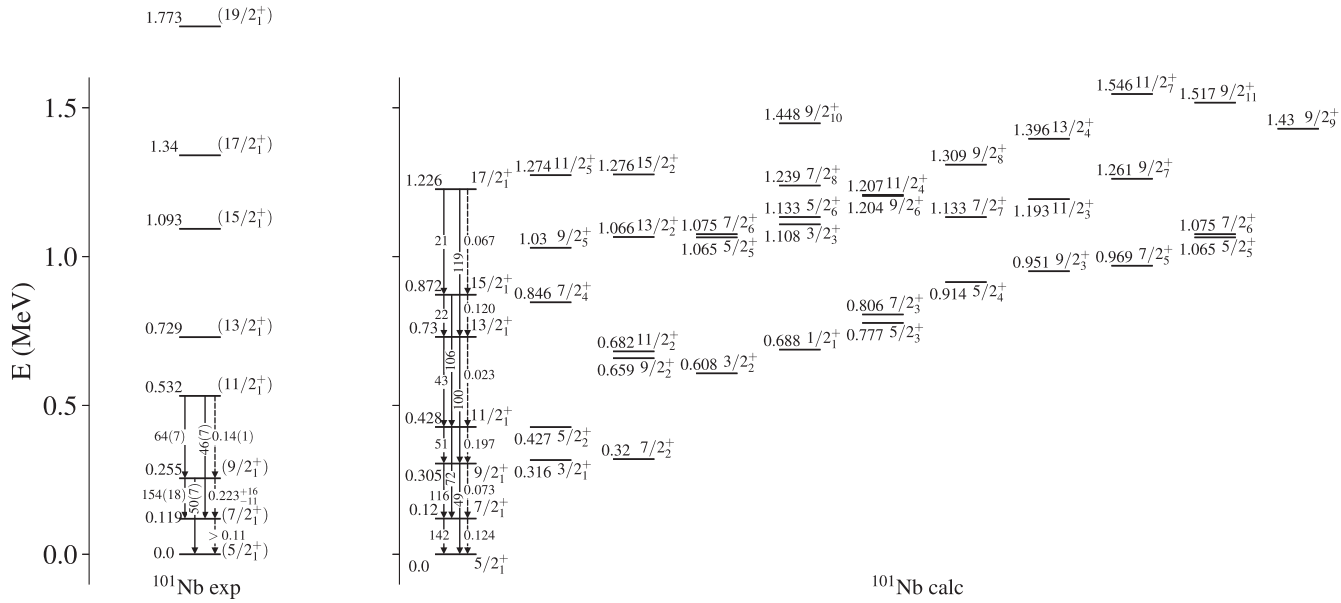

FIG. 7. Experimental and calculated energy levels in MeV, and $E2$ (solid arrows) and $M1$ (dashed arrows) transition rates in W.u. for ^{101}Nb. Shown are states that were assigned to different bands in the intruder configuration up to ≈1.5 MeV (a few other states not shown could not be associated with a certain band), except the $9/2^+_9$, which is normal. Data taken from [75,76].

(where the differences are 0.3, 0.212 MeV, respectively) to ^{97}Nb (where the difference is 0.422 MeV), suggesting the additional fermion increases collectivity, which reduces the energy of the $9/2^+_2$ state compared to the $0^+_{2;B}$ state of $^{92-96}$Zr. For ^{93}Nb, the observed $B(E2; 9/2^+_2 \rightarrow 9/2^+_1) = 1.03(9)$ W.u, is close to the calculated value 0.85 W.u., but is smaller than the observed value $B(E2; 9/2^+_3 \rightarrow 9/2^+_1) = 1.52(10)$ W.u., suggesting that the $9/2^+_2$ is associated with the B configuration, but that the mixing between these states is possibly stronger than predicted. This is contrary to previous works [50,74] that assigned the $9/2^+_2$ as part of the configuration A quintuplet. A similar situation occurs with $11/2^+_3$ state. The observed $B(E2; 11/2^+_3 \rightarrow 9/2^+_2) = 6(3)$ and $B(E2; 11/2^+_3 \rightarrow 9/2^+_3) = 5(2)$ W.u. suggest a fragmentation of the $11/2^+_3$ compared to the calculated values of 16 and 0.6 W.u., respectively. The observed value of $B(E2; 11/2^+_3 \rightarrow 11/2^+_1) = 21(7)$ W.u., which is calculated to be 0.1 W.u., suggests that this fragmentation is possibly due to stronger mixing between the $11/2^+$ states, also due to the stronger $B(E2; 11/2^+_2 \rightarrow 7/2^+_1) = 17(7)$. The strong $B(E2; 5/2^+_3 \rightarrow 7/2^+_1) = 90(35)$ [50], calculated to be weak (0.1) might suggest stronger mixing for either the $5/2^+_3$ or $7/2^+_1$ states.

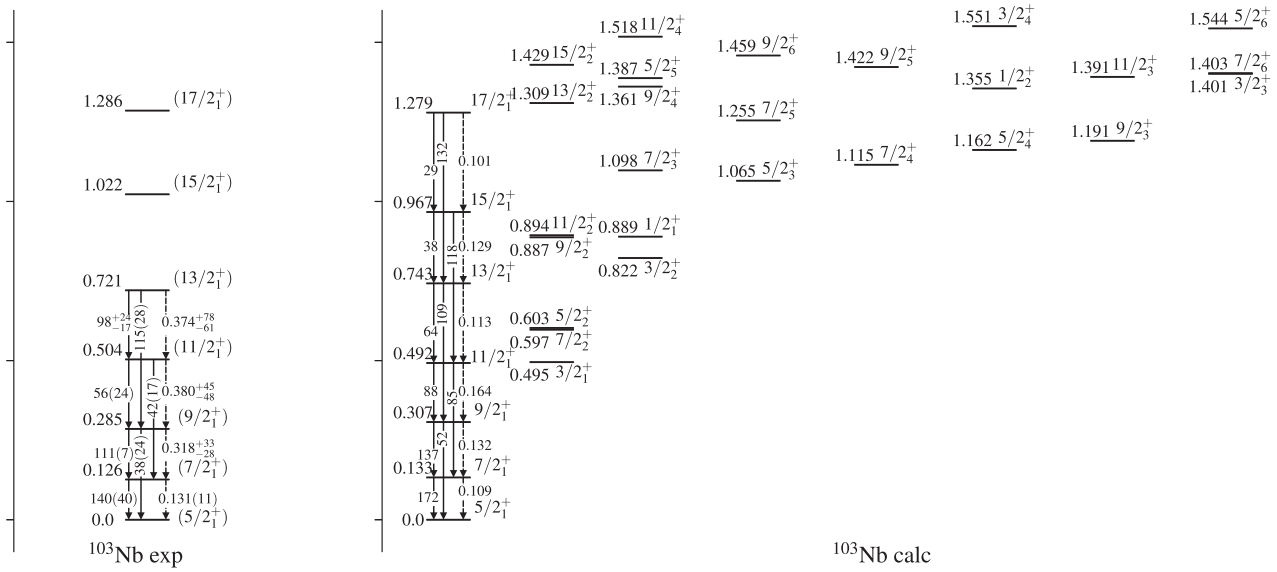

FIG. 8. Experimental and calculated energy levels in MeV, and $E2$ (solid arrows) and $M1$ (dashed arrows) transition rates in W.u. for ^{103}Nb. All states are assigned to the intruder configuration. Data taken from [76,77].

2. The $^{99-103}$Nb region: IQPT and strong coupling

For ^{99}Nb, shown in Fig. 6, the ground state is a result of the weak coupling between the $0^+_{1;\mathrm{A}}$ of the ^{98}Zr core and the $\pi(1g_{9/2})$ orbit. The higher lying states, however, are all intruder. This is in line with the case of ^{98}Zr, where some of the configuration B states lie below the first excited 2^+ of configuration A. For example, although mixing is stronger, the calculated $7/2^+_1$ has a large $n_d = 1$ component ($\gtrsim$60%), which associates it as part of the quintuplet that originates from the coupling of the $\pi(1g_{9/2})$ with the $2^+_{1;\mathrm{B}}$ of ^{98}Zr. The higher lying calculated states have larger n_d mixing. The calculated $7/2^+_1$ is lower in energy than the $9/2^+_2$, which is mainly composed of the coupling between the $\pi(1g_{9/2})$ and the $0^+_{2;\mathrm{B}}$ of ^{98}Zr. This is an example for the onset of deformation that has been identified in ^{98}Zr [10,12]. The few measured $E2$ and $M1$ transitions are reproduced qualitatively for the $B(E2; 5/2^+_1 \to 9/2^+_1) = 4.6(6)$ W.u. [1], $B(M1; 7/2^+_1 \to 9/2^+_1) = 0.031(13)$ W.u. [0.006] and $B(E2; 3/2^+_2 \to 5/2^+_1) > 45$ W.u. [51], where in square brackets are the calculated values.

For $^{101-103}$Nb, shown in Figs. 7 and 8, the yrast states belong to the intruder B configuration and are arranged in a $K^\pi = 5/2^+$ rotational band, with an established Nilsson model assignment $5/2^+[422]$ [78]. The band members can be interpreted in the strong coupling scheme, where a particle is coupled to an axially deformed core. The indicated states are obtained by coupling the $\pi(1g_{9/2})$ state to the ground band ($L = 0^+_1, 2^+_1, 4^+_1, \ldots$) of $^{100-102}$Zr, which are all part of the intruder B configuration. For ^{103}Nb, the calculation reproduces well the observed particle-rotor splitting, with a moment of inertia, Eq. (24), $B = 0.018$ MeV. For ^{101}Nb, the experimental levels follow a less rotational pattern. The experimental $E2$ and $M1$ transitions within the band of both $^{101-103}$Nb are reproduced well by the calculation. In Fig. 9, the trend in $E2$ transitions and quadrupole moments as a function of angular momentum J seems to be very similar to that of the geometric collective model, Eqs. (26a) and (25a). The trend of the $M1$ transitions and magnetic moments is less similar, as these observables are less collective in nature and are strongly affected by the single-particle character of the wave function.

Besides the calculated ground state band, there are different K^π bands for which states are grouped together according to strong $E2$ transitions between them. The rightmost one of them in Fig. 7 of ^{101}Nb is the $9/2^+_9$ state, which is spherical with about 76% for the $n_d = 0$ component. Therefore, one can observe the change of configuration in the ground state, from A to B (Type II QPT), and also a change in the B configuration from spherical spectrum, beginning at ^{99}Nb, to deformed in ^{101}Nb (Type I QPT).

Altogether, there is an evolution of structure from weak coupling of a spherical shape in ^{93}Nb to strong coupling of a deformed shape in ^{103}Nb. Such shape changes within the B configuration (Type I QPT), superimposed on an abrupt configuration crossing (Type-II QPT), are the key defining feature of intertwined QPTs (IQPTs). Interestingly, the intricate IQPTs scenario, originally observed in the even-even Zr isotopes [10,12], persists in the adjacent odd-even Nb isotopes.

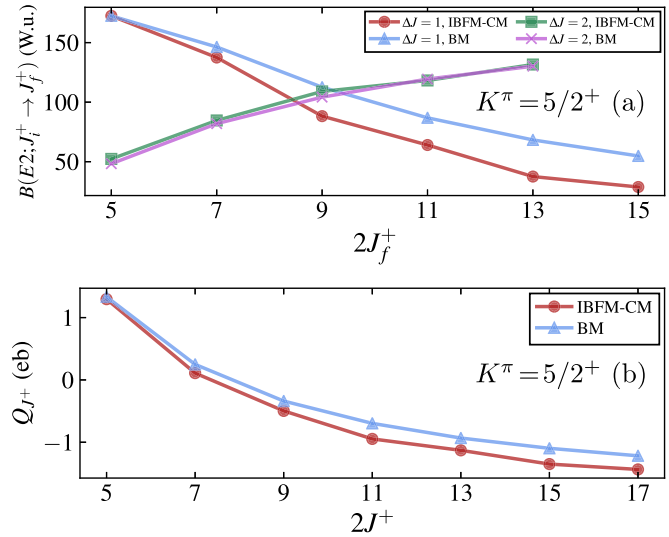

FIG. 9. Comparison between the present calculation and the Bohr and Mottelson model (BM). (a) $E2$ transition rates in W.u. between members of the $K^\pi = 5/2^+$ band of ^{103}Nb calculated in this work and using the collective model (BM), Eq. (26a), with $\Delta J = J_f - J_i$. (b) Quadrupole moments in eb for members of the $K^\pi = 5/2^+$ band in ^{103}Nb calculated in this work and using the collective model, Eq. (25a).

B. Negative-parity states

For the negative parity states, the individual isotopes are divided to two regions: a weak coupling region for $^{93-97}$Nb and the IQPT region for $^{99-103}$Nb, which also incorporates strong coupling.

For the region of $^{93-97}$Nb the calculation is compared to the experimental levels in Figs. 10–12. For each isotope, the lowest levels with $J^\pi = 1/2^-, 3/2^-, 5/2^-$ in each configuration are associated with the single-particle orbits $j = \pi(2p_{1/2}), \pi(2p_{3/2}), \pi(1f_{5/2})$.

For the region of $^{99-103}$Nb the calculation is compared to the experimental levels in Figs. 14–16. For each isotope the spectrum exhibits rotational bands that belong to the intruder B configuration, except in ^{99}Nb where the normal A configuration can be identified.

1. The $^{93-97}$Nb region: Weak coupling

As shown in Figs. 10–12, the levels with $J^\pi = 1/2^-_1, 3/2^-_1, 5/2^-_1$ in $^{93-97}$Nb have a quasiparticle character. They originate from the coupling of the $0^+_{1;\mathrm{A}}$ of the adjacent $^{92-96}$Zr isotopes with the $\pi(2p_{1/2}), \pi(2p_{3/2}), \pi(1f_{5/2})$ orbits, and are clearly identified in the calculation with a good agreement to the data. On top of each of them are other levels that have a large component $P_j^{(N_i,J)}$ of Eq. (21), with the same single-particle j-orbit, where $i = \mathrm{A}$ or B and J is the total angular momentum. However, these higher lying states are more mixed between the different configurations. For ^{93}Nb in Fig. 10 the single quasiparticle levels that are associated with configuration B can be identified in the experimental spectrum—the $(1/2^-, 3/2^-)$, $(1/2^-, 3/2^-)$ and $5/2^-_3$ state at energy 0.97, 1.29, and 1.37 MeV, respectively. They are reproduced well by

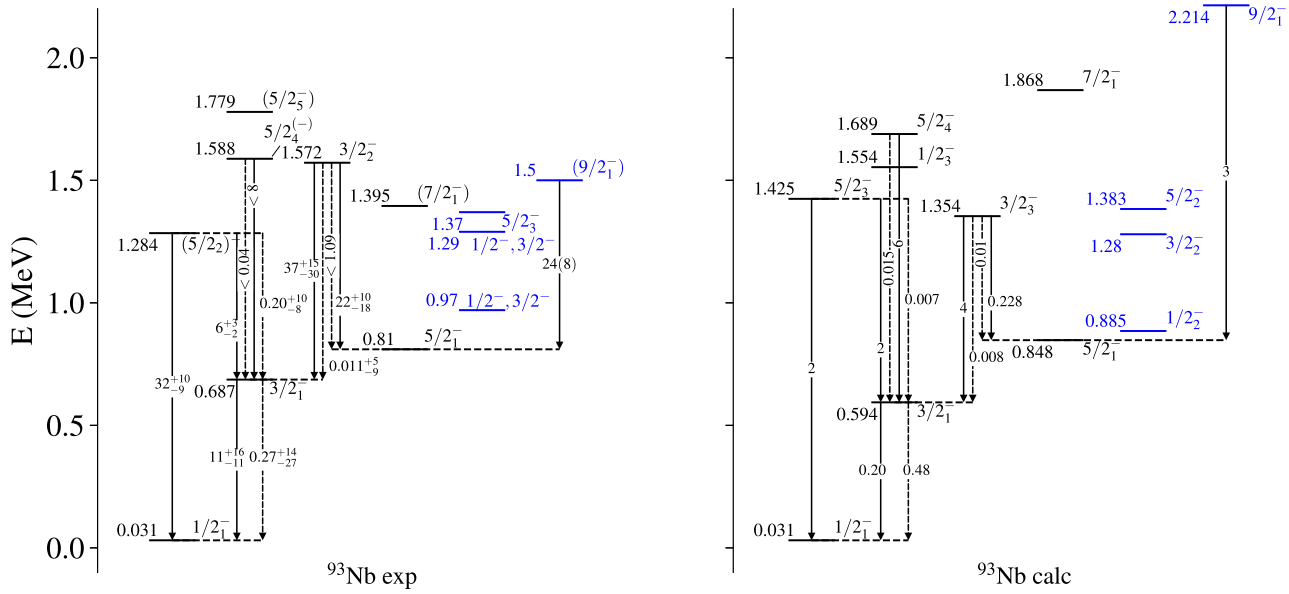

FIG. 10. Experimental (left) and calculated (right) energy levels in MeV, and $E2$ (solid arrows) and $M1$ (dashed arrows) transition rates in W.u., for ^{93}Nb. Data taken from [50,70].

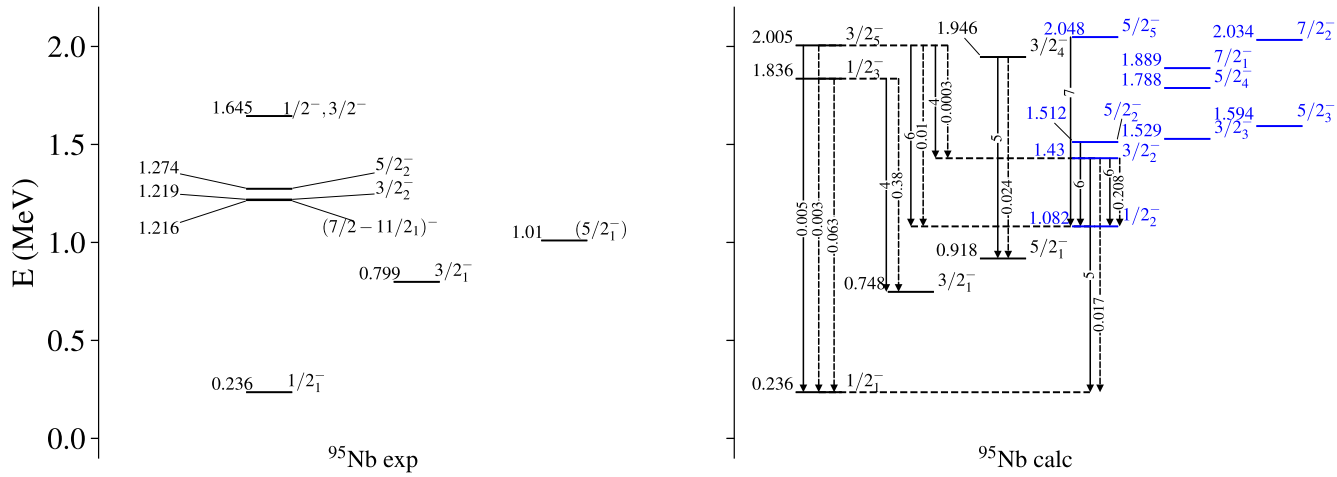

FIG. 11. Experimental (left) and calculated (right) energy levels in MeV, and $E2$ (solid arrows) and $M1$ (dashed arrows) transition rates in W.u., for ^{95}Nb. Normal (intruder) states are depicted in black (blue). Data taken from [71].

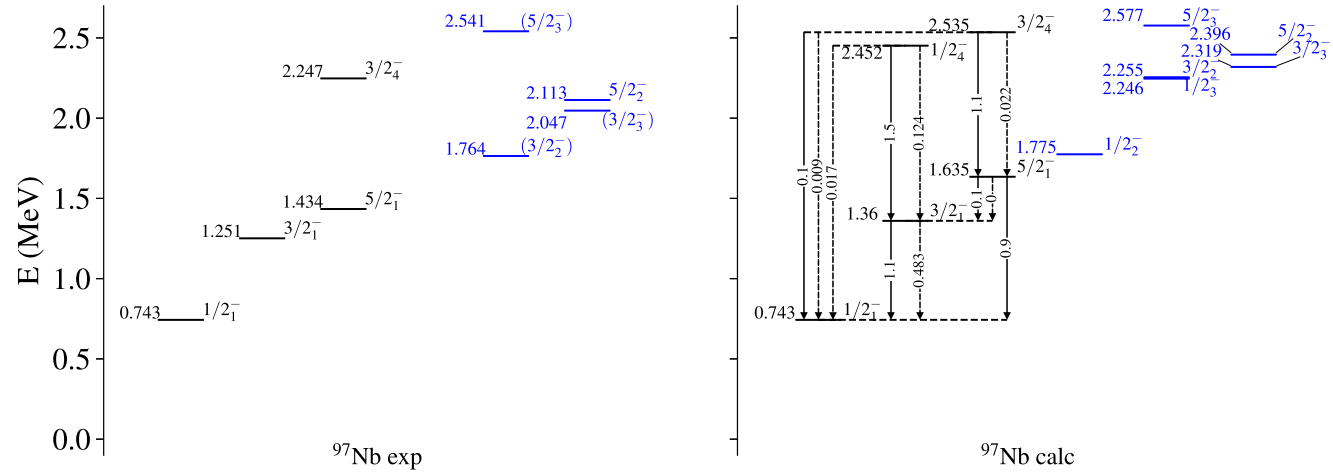

FIG. 12. Experimental (left) and calculated (right) energy levels in MeV, and $E2$ (solid arrows) and $M1$ (dashed arrows) transition rates in W.u., for ^{97}Nb. Normal (intruder) states are depicted in black (blue). Data taken from [72].

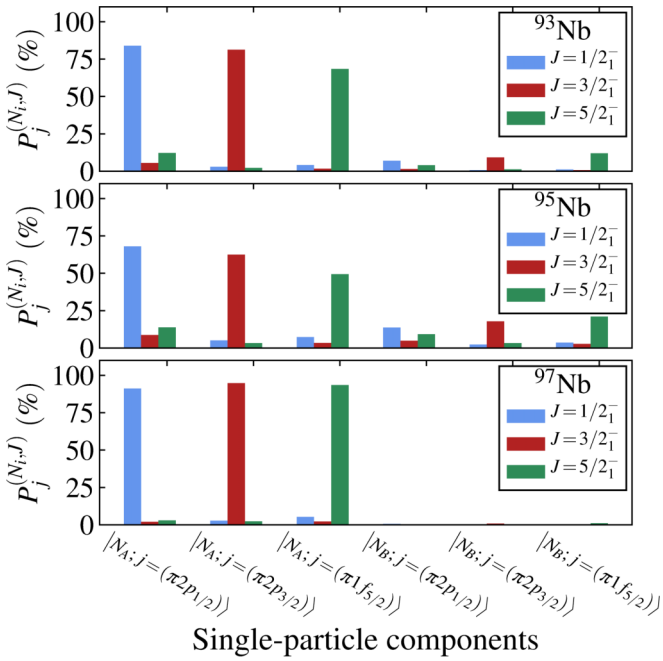

FIG. 13. Percentage of the single-particle components of the normal A and intruder B configurations, Eq. (21), for the calculated $1/2_1^-, 3/2_1^-, 5/2_1^-$ states of $^{93-97}$Nb isotopes.

the calculation, depicted in blue in Fig. 10. For ^{95}Nb, Fig. 11, there are not enough data to identify configuration B states, and for ^{97}Nb some states could possibly belong as well to configuration B, as depicted in Fig. 12.

$E2$ transitions are measured only for ^{93}Nb and are reproduced more qualitatively rather than quantitatively, where some of them are large and at variance with the calculation (written in square brackets), $B(E2;5/2_2^- \to 1/2_1^-) = 32^{+10}_{-9}$ W.u. [2], $B(E2;3/2_2^- \to 3/2_1^-) = 37^{+15}_{-30}$ W.u. [4] and $B(E2;9/2_1^- \to 5/2_1^-) = 24(8)$ W.u. [3]. The first value of the $5/2_2^- \to 1/2_1^-$ is surprising due to the small value of the $B(E2;2_1^+ \to 0_1^+) = 6.4(6)$ W.u. of the core, ^{92}Zr, which is expected to be comparable in the weak coupling scenario. They might also suggest a more unique mixing between the individual orbits, which is not considered in this work for simplicity. On the other hand, $M1$ transitions, measured only for ^{93}Nb, are all reproduced by the calculation to a good degree. The latter confirms the calculated orbital structure of the states involved in theses transitions—the $1/2_1^-, 3/2_1^-, 5/2_1^-$ states have large $P^{(N_A,1/2_1^-)}_{\pi(2p_{1/2})}, P^{(N_A,3/2_1^-)}_{\pi(2p_{3/2})}, P^{(N_A,5/2_1^-)}_{\pi(1f_{5/2})}$ probabilities, and the calculated $3/2_3^-, 5/2_3^-, 5/2_4^-$ states have large $P^{(N_A,3/2_3^-)}_{\pi(2p_{1/2})}, P^{(N_A,5/2_3^-)}_{\pi(2p_{1/2})}, P^{(N_A,5/2_4^-)}_{\pi(2p_{3/2})}$ probabilities, respectively.

Wave functions. For $^{93-97}$Nb, as shown in Fig. 13, the lowest state $1/2_1^-$ has a dominant $\pi(2p_{1/2})$ component of the normal A configuration, $P^{(N_A,1/2_1^-)}_{\pi(2p_{1/2})} \approx 80\%, 70\%, 90\%$, with weak mixing between the different single-particle components of each of the configurations. A similar trend is observed for the $3/2_1^-$ and $5/2_1^-$ states, indicating these three states are single-quasiparticle excitations of the $\pi(2p_{1/2}), \pi(2p_{3/2}), \pi(1f_{5/2})$ orbits, coupled to the normal A configuration. The reason the latter $P_j^{(N_A,J)}$ probabilities are smaller in ^{95}Nb is due to the slightly larger mixing between the configurations in the even-even ^{94}Zr core, compared to ^{92}Zr (the core of ^{93}Nb) and ^{96}Zr (the core of ^{97}Nb) [12].

2. The $^{99-103}$Nb region: Strong coupling

As shown in Figs. 14–16, one can identify rotational bands with $K^\pi = 3/2^-$ and $5/2^-$ in $^{99-103}$Nb. For ^{99}Nb, the $1/2_1^-$ is identified as the configuration A normal state that originates from the coupling of the $\pi(2p_{1/2})$ orbit with the $0^+_{1;A}$ state of the adjacent ^{98}Zr isotope. Alongside it, there is a rotational band with $K^\pi = 3/2^-$ that the calculation reproduces to a reasonable degree; however, a calculated $1/2_2^-$ appears in the spectrum, making this a $K^\pi = 1/2^-$ band. Alongside this band, the calculation suggests another $K^\pi = 1/2^-$ band beginning at 0.745 MeV. The $E2$ transitions within these bands are relatively stronger than those built upon the $1/2_1^-$ state, as expected from a rotational band. The large $E2$ transitions between the two $K^\pi = 1/2_2^-, 1/2_3^-$ bands indicate a strong mixing between them. For $M1$ transitions, the calculation in Fig. 14 depicts strong ones between some of the $3/2^-$ and $1/2^-$ states. The $3/2_3^- \to 1/2_1^-$ is large since it is a transition between states of the same configuration A with dominant $\pi(2p_3/2)$ and $\pi(2p_1/2)$ components, respectively. The $3/2_2^-$ state, which is mixed with the $3/2_3^-$, has therefore also a stronger transition to the $1/2_1^-$. The $3/2_1^-$ has an almost zero configuration A $\pi(2p_3/2)$ component, which does not connect strongly to the $1/2_1^-$ (see discussion on the wave functions below for more details).

For ^{101,103}Nb, all the states belong to the intruder B configuration and are arranged in two rotational bands with $K^\pi = 3/2^-, 5/2^-$, with a Nilsson model assignment $3/2^-[301]$, $5/2^-[303]$. The calculation also suggests an additional $K^\pi = 1/2^-$ band alongside them with large staggering. For ^{101}Nb, the calculated $K^\pi = 3/2^-, 5/2^-$ bands are a little higher in energy than experiment and the $K^\pi = 3/2^-$ band is somewhat staggered. For ^{103}Nb, the agreement with experiment is excellent, with a clear particle-rotor splitting of the energy, and with moments of inertia, Eq. (24), $B = 0.022, 0.024$ MeV for the $K^\pi = 5/2^-, 3/2^-$ bands, respectively. The $E2$ and $M1$ transitions within the bands of both ^{101,103}Nb are reproduced well. The trend of the $E2$ transitions, alongside the trend of the quadrupole moment, as a function of angular momentum J, is seen in Fig. 17 to be very similar with that of the geometric collective model, Eqs. (26a) and (25a). As in the positive-parity case, Sec. IV A 2, the trend of the $M1$ transitions and magnetic moments is less similar. The change in the experimental $K^\pi = 3/2_1^-$ to a calculated $K^\pi = 1/2_2^-$ band in ^{99}Nb and the additional calculated $K^\pi = 1/2_1^-$ that do not appear in the spectrum might suggest the need to modify the proton single-particle energies used in the BCS calculation.

Wave functions. As shown in Fig. 18, for ^{99}Nb, the lowest state $1/2_1^-$ has a dominant $\pi(2p_{1/2})$ component of the normal A configuration, $P^{(N_A,1/2_1^-)}_{\pi(2p_{1/2})} \approx 75\%$, with weak mixing between the different single-particle components of each of

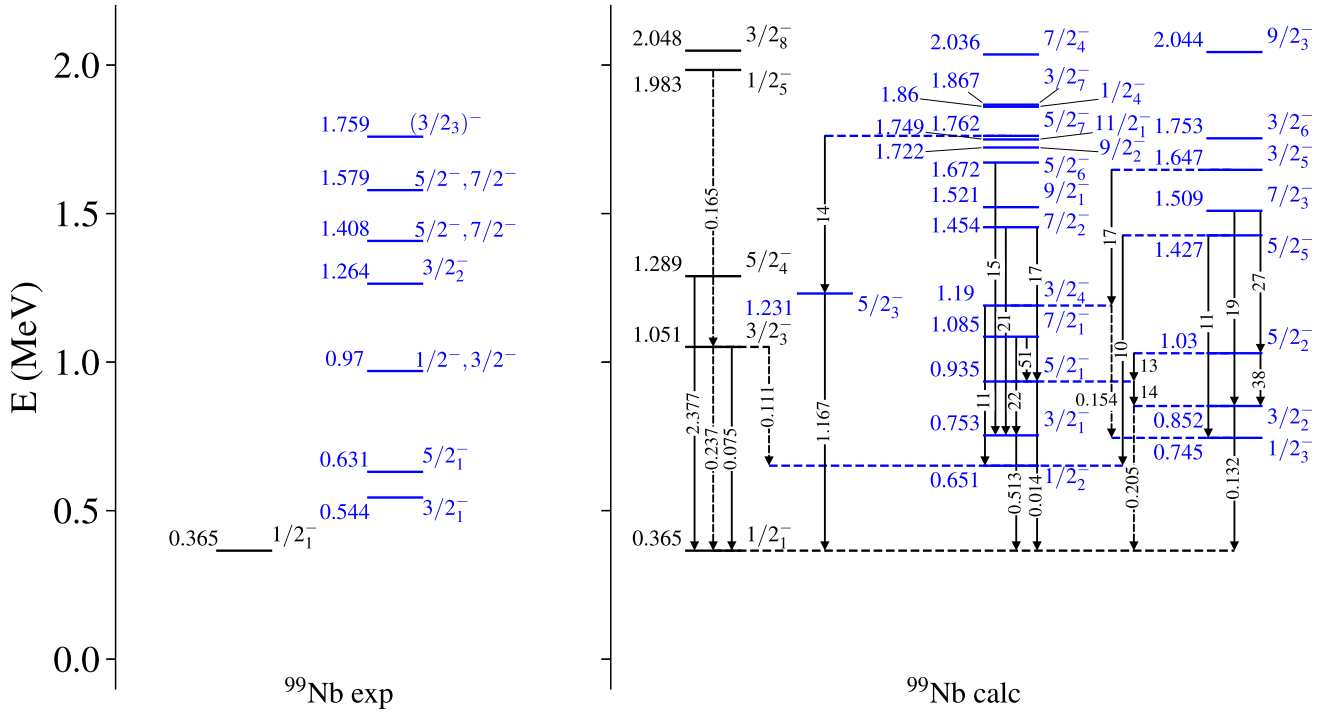

FIG. 14. Experimental (left) and calculated (right) energy levels in MeV, and $E2$ (solid arrows) and $M1$ (dashed arrows) transition rates in W.u., for ^{99}Nb. Other calculated $M1$ transitions, not shown in the figure, are smaller than 0.1 W.u. Normal (intruder) states are depicted in black (blue). Data taken from [73].

the configurations. This $1/2_1^-$ is the lowest configuration A state that resides alongside the intruder B configuration. The $5/2_1^-$ state has a dominant $\pi(1f_{5/2})$ B configuration component, while the $3/2_1^-$ is mixed between the intruder B configuration $\pi(2p_{3/2})$ and $\pi(2f_{5/2})$ components. The $3/2_3^-$ state (not shown in Fig. 18) is the one with large $P^{(N_A,3/2_3^-)}_{\pi(2p_{3/2})} \approx 68\%$ and $P^{(N_B,3/2_3^-)}_{\pi(2p_{3/2})} \approx 21\%$, while the $3/2_2^-$ has almost exactly the opposite values for these components. For ^{101,103}Nb, both the $1/2_1^-$ and $3/2_1^-$ states are mixed between the intruder B configuration $\pi(2p_{3/2})$ and $\pi(1f_{5/2})$ components, while the $5/2_1^-$ has a dominant $\pi(1f_{5/2})$ component.

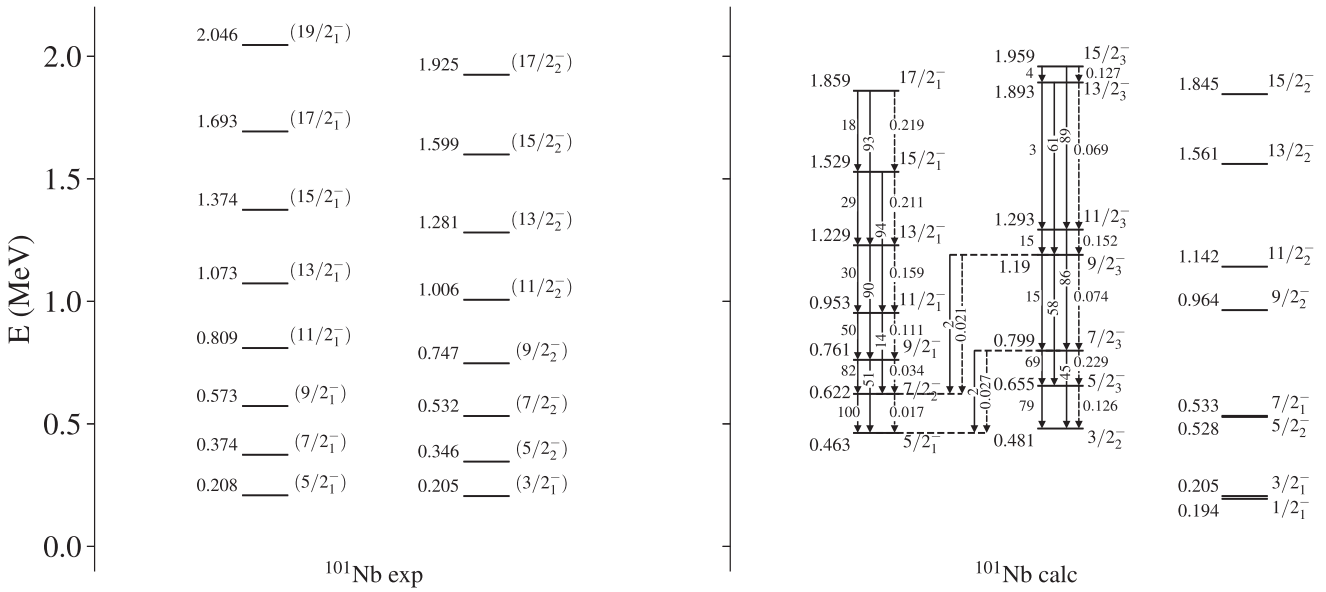

FIG. 15. Experimental (left) and calculated (right) energy levels in MeV, and $E2$ (solid arrows) and $M1$ (dashed arrows) transition rates in W.u., for ^{101}Nb. Data taken from [79].

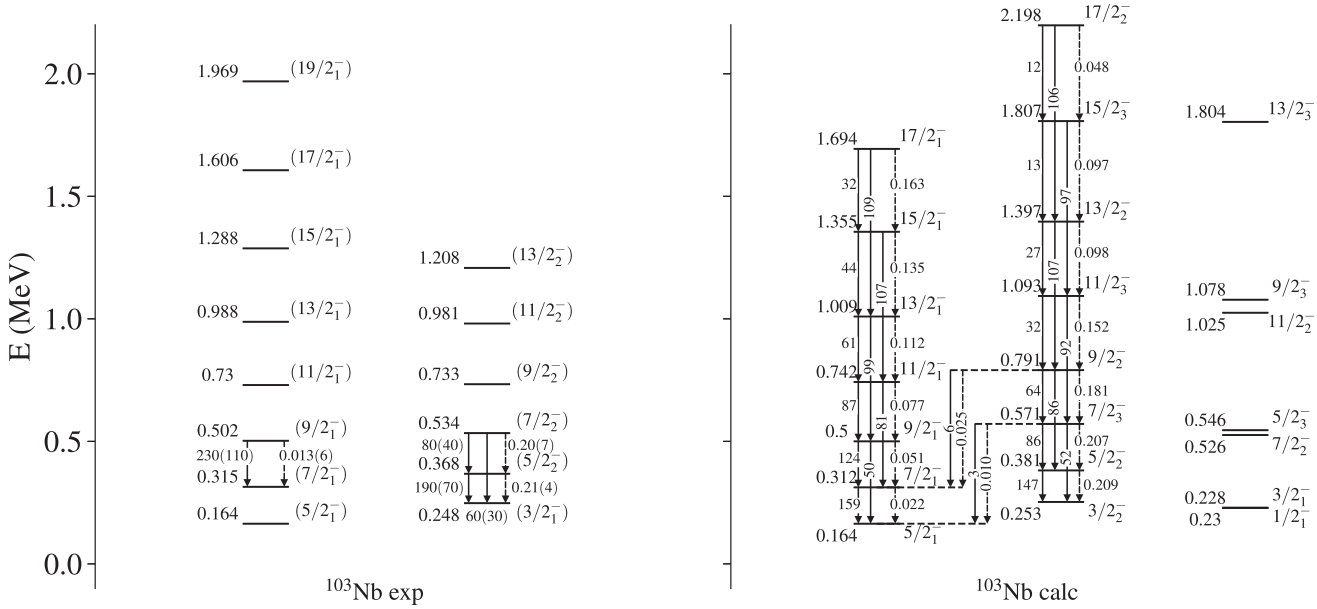

FIG. 16. Experimental (left) and calculated (right) energy levels in MeV, and $E2$ (solid arrows) and $M1$ (dashed arrows) transition rates in W.u., for ^{103}Nb. Data taken from [77].

V. RESULTS: EVOLUTION OF WAVE FUNCTIONS AND OBSERVABLES ALONG THE NIOBIUM CHAIN

A. Evolution of configuration and single-particle content

A possible change in the angular momentum of the ground state (J_{gs}) is a characteristic signature of QPTs in odd-mass nuclei, unlike even-even nuclei where the ground state remains 0^+ after the crossing. It is an important measure for the quality of the calculations. A mean-field approach, for example, without configuration mixing, fails to reproduce the change between the $9/2^+_1$ and $5/2^+_1$ states in J^+_{gs} for the Nb isotopes [32]. Information on configuration changes for each isotope can be inferred from the evolution of the probabilities $P^{(N_A,J)}$ or $P^{(N_B,J)}$, Eq. (20), of the states considered. Figure 19 shows the percentage of the wave function within the B configuration, in panel (a) for the ground state (J^+_{gs}) and first-excited state ($7/2^+_1$) and in panel (b) for the

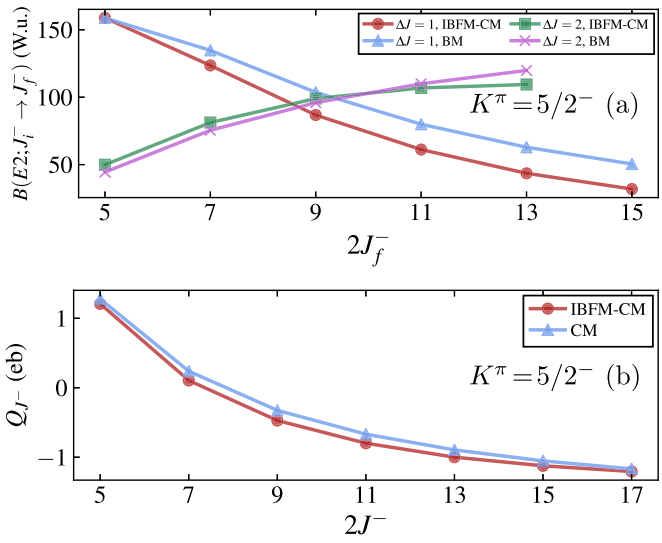

FIG. 17. Comparison between the present calculation and the Bohr and Mottelson model (BM). (a) $E2$ transition rates in W.u. between members of the $K^\pi = 5/2^-$ band of ^{103}Nb calculated in this work and using the collective model (BM), Eq. (26a), with $\Delta J = J_f - J_i$. (b) Quadrupole moments in eb for members of the $K^\pi = 5/2^-$ band in ^{103}Nb calculated in this work and using the collective model, Eq. (25a).

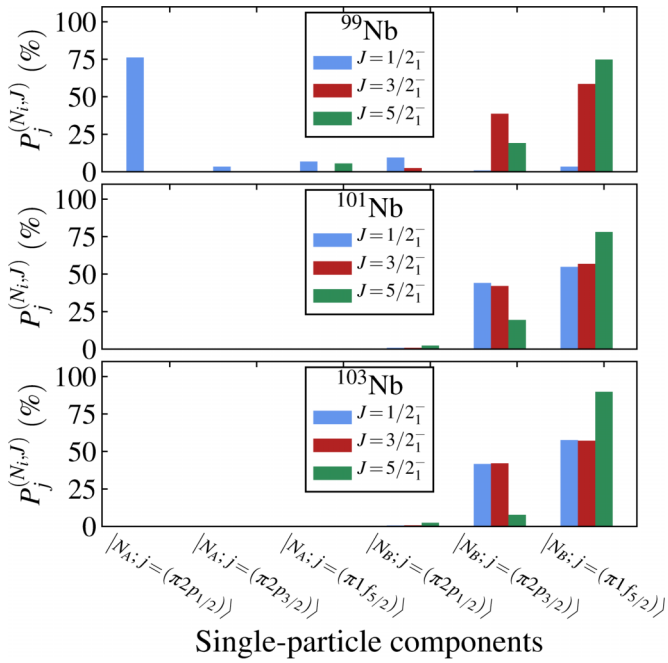

FIG. 18. Percentage of the single-particle components of the normal A and intruder B configurations, Eq. (21), for the calculated $1/2^-_1$, $3/2^-_1$, $5/2^-_1$ states in $^{93-97}$Nb isotopes.

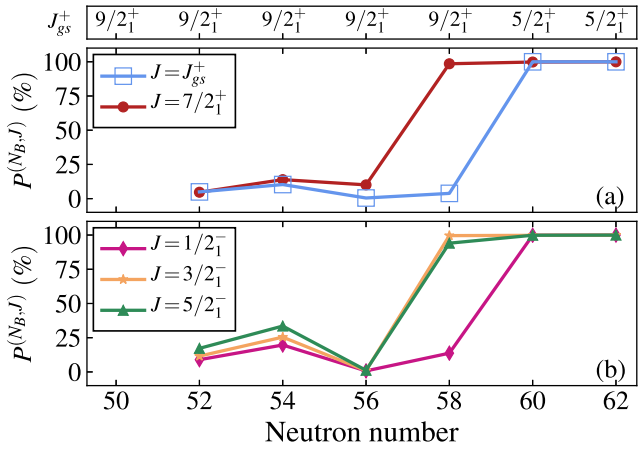

FIG. 19. Percentage of the intruder (B) component [the $P^{(N_B,J)}$ probability in Eq. (20)] for $^{93-103}$Nb. (a) The ground state (J^+_{gs}) and the first-excited positive-parity state ($7/2^+_1$). (b) The $1/2^-_1$, $3/2^-_1$, $5/2^-_1$ states for the negative-parity states. The values of J^+_{gs} are indicated at the top panel.

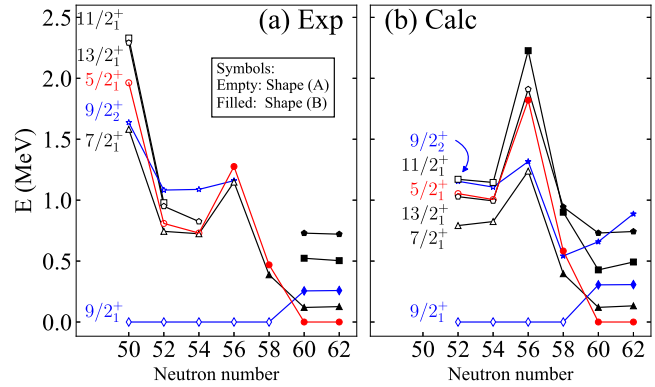

FIG. 20. Comparison between (a) experimental [70–73,80] and (b) calculated lowest-energy positive-parity levels in Nb isotopes. Empty (filled) symbols indicate a state dominated by the normal A configuration (intruder B configuration), with assignments based on Eq. (20). In particular, the $9/2^+_1$ state is in the A (B) configuration for neutron number 52–58 (60–64) and the $5/2^+_1$ state is in the A (B) configuration for 52–54 (56–64). Note that the calculated values start at 52, while the experimental values include the closed shell at 50.

$J = 1/2^-_1, 3/2^-_1, 5/2^-_1$ states, as a function of neutron number across the Nb chain. The rapid change in structure of the J^+_{gs} and $1/2^-_1$ states from the normal A configuration (small $P^{(N_B,J)}$ probability) for neutron number 52–58 ($^{93-99}$Nb) to the intruder B configuration (large $P^{(N_B,J)}$ probability) for neutron number 60–62 ($^{101-103}$Nb) is clearly evident, signaling a Type II QPT, as mentioned in Sections IV A 2 and IV B 2. The configuration change appears sooner in the $7/2^+_1$ and $3/2^-_1, 5/2^-_1$ states, which switch to configuration B already at neutron number 58 (^{99}Nb). The behavior of the J_{gs}, $1/2^-_1$ and $7/2^+_1, 3/2^-_1, 5/2^-_1$ states is in line with the behavior of the 0^+_1 and 2^+_1 states of the $_{40}$Zr cores with the same neutron numbers [10,12], which also change from configuration A to B at neutron number 60 and 58, respectively (see Fig. 10 of Ref. [12]). Outside a narrow region near neutron number 60, where the crossing occurs, the two configurations are weakly mixed and the states retain a high level of purity, except for the negative parity states for neutron number 54 (^{95}Nb), where the mixing is somewhat stronger.

B. Energy levels

Figures 20–21 show the experimental and calculated levels of selected positive- and negative-parity states, respectively, along with assignments to configurations based on Eq. (20). Open (solid) symbols indicate a dominantly normal (intruder) state with small (large) $P^{(N_B,J)}$ probability. For the positive-parity states of Fig. 20, in the region between neutron number 50 and 56, there appear to be two sets of levels with a weakly deformed structure, associated with configurations A and B. All levels decrease in energy for 52–54, away from the closed shell, and rise again at 56 due to the $\nu(2d_{5/2})$ subshell closure. At neutron number 58, there is a pronounced drop in energy for the states of the B configuration, due to the onset of deformation. At 60, the two configurations cross, indicating a Type II QPT, and the ground state changes from $9/2^+_1$ to $5/2^+_1$, becoming the bandhead of a $K^\pi = 5/2^+$ rotational band composed of $5/2^+_1, 7/2^+_1, 9/2^+_1, 11/2^+_1, 13/2^+_1, \ldots$ states. Beyond neutron number 60, the intruder B configuration remains strongly deformed and the band structure persists. The above trend is similar to that encountered in the even-even $_{40}$Zr cores (see Fig. 14 of Ref. [12]).

For the negative-parity states in Fig. 21, in the region between neutron number 50 and 56, there appear to be the $1/2^-_1$ state and two sets of levels for each of the $3/2^-$ and $5/2^-$ states with a weakly deformed structure, associated with configurations A and B. All levels decrease in energy for 52–54, away from the closed shell, and rise again at 56 due to the $\nu(2d_{5/2})$ subshell closure. From 58, there is a pronounced drop in energy for the states of the B configuration, due to the onset of deformation. At 60, the two configurations cross, indicating a Type II QPT. The calculated normal $1/2^-$ rises in energy

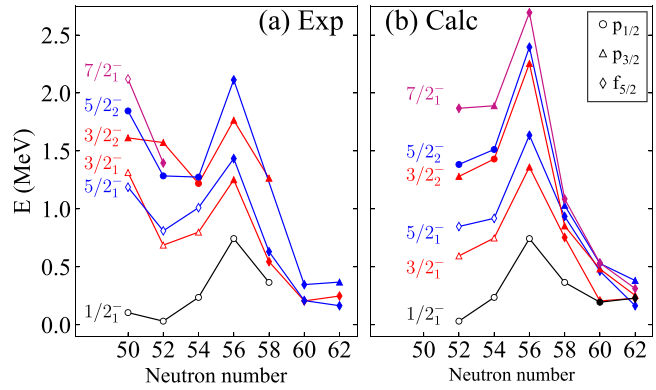

FIG. 21. Comparison between (a) experimental [70–73,80] and (b) calculated lowest-energy negative-parity levels in Nb isotopes. Empty (filled) symbols indicate a state dominated by the normal A configuration (intruder B configuration), with assignments based on Eq. (20). Note that the calculated values start at 52, while the experimental values include the closed shell at 50.

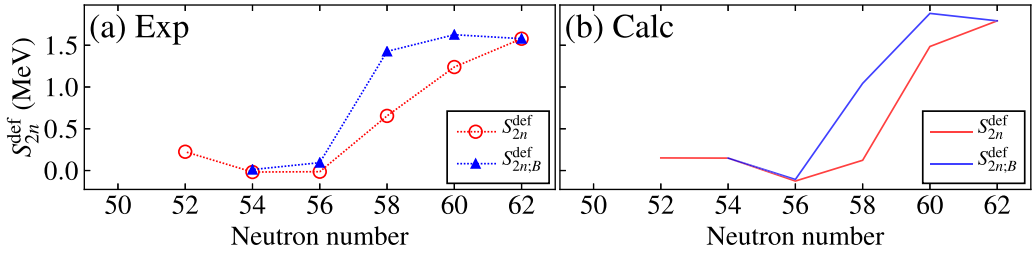

FIG. 22. Comparison of the deformed part of the two-neutron separation energies, ($S_{2n}^{\rm def}$), between (a) experiment [81] and (b) calculation.

and the $1/2_1^-$ remains the lowest negative-parity state in ^{101}Nb and at ^{103}Nb it is the $5/2_1^-$ that is lowest. Although not in the experimental data, the trend of the $1/2_1^-$ state seems to suggest the existence of a low-lying $1/2^-$ also in ^{101,103}Nb, as suggested by the calculation. The $1/2_1^-$, $3/2_1^-$, and $5/2_1^-$ states become the bandheads of $K^\pi = 1/2^-, 3/2^-, 5/2^-$ rotational bands, respectively.

C. Two-neutron separation energy

An observable that portrays both types of QPTs is two-neutron separation energy, defined as

$$S_{2n} = 2M_n + M(N-2,Z) - M(N,Z), \tag{27}$$

where $M(N,Z)$ is the mass of a nuclei with N,Z neutrons and protons, respectively, and M_n is the neutron mass. It is convenient to transcribe the S_{2n} as

$$S_{2n} = -\tilde{A} - \tilde{B}N_v \pm S_{2n}^{\rm def} - \Delta_n, \tag{28}$$

where N_v is half the number of valence particles in the boson core and $S_{2n}^{\rm def}$ is the contribution of the deformation, obtained by the expectation value of the Hamiltonian in the ground state. The $+$ sign applies to particles and the $-$ sign to holes. The Δ_n parameter takes into account the neutron subshell closure at 56, $\Delta_n = 0$ for 50–56, and $\Delta_n = 2$ MeV for 58–62. For the Nb isotopes, the chosen values in Eq. (28) are $\tilde{A} = -17.25$, $\tilde{B} = 0.758$ MeV. The value of $\tilde{A}$ is taken to fit ^{91}Nb, and the values of $\tilde{B}$ and Δ_n are taken from the previous even-even Zr calculation [12]. In Fig. 22, the experimental (left) and calculated (right) deformed part, $S_{2n}^{\rm def}$ [24,25], are shown in red circles and lines, respectively. $S_{2n}^{\rm def}$ is obtained by subtracting the linear part and Δ_n from the experimental and calculated S_{2n}. One can clearly see the onset of deformation going from neutron number 52–56, where $S_{2n}^{\rm def}$ is small, to 58–62, where it jumps and rises.

In order to denote the occurrence of both Type I and II QPTs, in addition to Eq. (28), it is also possible using Eq. (27) to estimate two-neutron separation energies for excited states by using the mass of an excited state $M(N,Z) \equiv M_{\rm exc}(N,Z) = M_{\rm gs}(N,Z) + E_{\rm exc}(N,Z)$, where $M_{\rm gs}(N,Z)$ is the mass for the ground state and $E_{\rm exc}(N,Z)$ is the energy of the excited state. Therefore, adding the difference $E_{\rm exc}(N-2,Z) - E_{\rm exc}(N,Z)$ to Eqs. (27) and (28) gives the two-neutron separation energy for an excited state, and for this the lowest configuration B state is chosen. The experimental and calculated results, $S_{2n;\rm B}^{\rm def}$, are given in blue triangles (left) and lines (right), respectively, in Fig. 22. It is seen that for neutron number 54–56 $S_{2n;\rm B}^{\rm def}$ is small, then at 58 it jumps due to the onset of deformation at 60, then it flattens. This behavior denotes the Type I QPT of shape evolution from spherical to axially deformed, within configuration B. It is similar to the behavior of the $_{61}$Pm, $_{63}$Eu, and $_{65}$Tb isotopes, which also undergo a QPT from spherical to axially deformed shape [24,25]. For neutron number 54–56, $S_{2n;\rm B}^{\rm def}$ (triangles) is close to the value of $S_{2n}^{\rm def}$ (circles), as configuration B is more spherical. At 58, there is a larger jump than $S_{2n}^{\rm def}$ since configuration B is more deformed than A, which continues at 60. For 62, both $S_{2n;\rm B}^{\rm def}$ and $S_{2n}^{\rm def}$ coincide since the ground state is configuration B, which denotes the Type II QPT. Therefore, the deformed part of the two-neutron separation energies in its ground and excited states serves as an important indicator for the occurrence of IQPTs.

D. $E2$ transition rates and quadrupole moments

Electromagnetic transitions and moments provide further insight into the nature of QPTs. Figure 23 shows $B(E2; 7/2_1^+ \to J_{\rm gs}^+)$ in panel (a) and quadrupole moment of $J_{\rm gs}^+$ in panel (b). These observables are related to the deformation, the order parameter of the QPT. Although the data are incomplete, one can still observe small (large) values of these observables below (above) neutron number 60, indicating an increase in deformation. The calculation reproduces well this trend and attributes it to a Type II QPT involving a jump between neutron number 58 and 60, from a weakly deformed

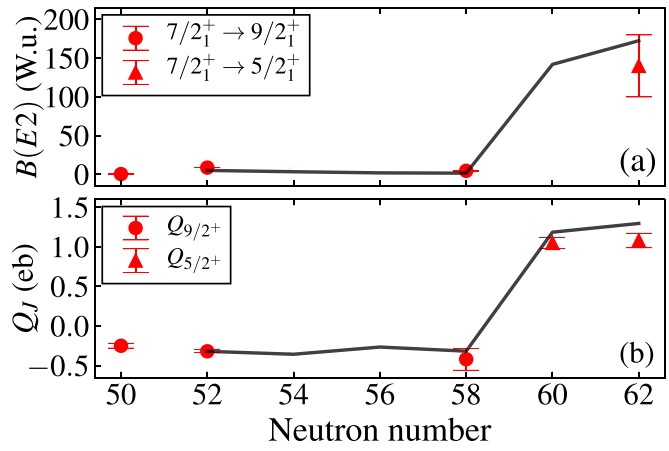

FIG. 23. Evolution of (a) $B(E2; 7/2_1^+ \to J_{\rm gs}^+)$ in W.u. and (b) Quadrupole moments of $J_{\rm gs}^+$ in eb. Symbols (solid lines) denote experimental data (calculated results). Data in panels (a) and (b) are taken from [70,77,80] and [70,80,82], respectively.

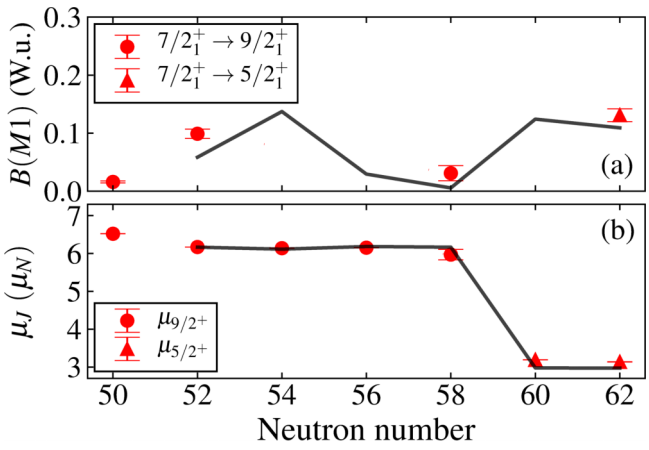

FIG. 24. Evolution of (a) $B(M1; 7/2^+ \to J^+_{gs})$ in W.u. and (b) Magnetic moments of J^+_{gs} in eb. Symbols (solid lines) denote experimental data (calculated results). Data in panels (a) and (b) are taken from [70,73,77,80] and [82], respectively.

A configuration, to a strongly deformed B configuration. The trend in the $E2$ transition rates is very similar to that of the $2^+_1 \to 0^+_1$ transition of the adjacent even-even Zr isotopes. In the Zr case, the sudden increase at neutron number 60 is ascribed to the IQPT, where the ground state configuration changes from normal to intruder, while the intruder configuration evolves at the same time from being quasispherical to deformed [10,12].

E. $M1$ transitions and magnetic moments

The trend in the experimental $B(M1; 7/2^+_1 \to J^+_{gs})$, shown in Fig. 24(a), suggests a jump at neutron number 52 and another one at 62, which is reproduced by the calculation to a good degree. This suggests that $M1$ transition rates might be an observable that indicates less the Type II QPT, possibly due to their sensitivity to the single-particle degrees of freedom rather than the collective ones. However, the Type II scenario is strongly supported by the trend of the magnetic moments (μ_J) of the ground state, shown in Fig. 24(b), where both the data and the calculation show a constant value of μ_J for neutron number 52–58, and a drop to a lower value at 60, which persists for 60–62. This trend of approximately constant value for each range of neutron numbers, suggests a corresponding constant mixing in the ground state wave function, in line with the calculated weak mixing before and after the crossing.

VI. CONCLUSIONS AND OUTLOOK

The general framework of the interacting boson-fermion model with configuration mixing (IBFM-CM) has been presented, allowing a quantitative description of shape coexistence, configuration mixing, and related QPTs in odd-mass nuclei. A quantal analysis for the chain of the odd-even $_{41}$Nb isotopes involving positive- and negative-parity states was performed for neutron number 52–62. It examined the spectra and properties of individual isotopes as well as the evolution of energy levels and other observables (two-neutron separation energies, $E2$ and $M1$ transition rates, and magnetic and quadrupole moments) along the chain. Special attention has been devoted to changes in the configuration-content and single-particle-content of wave functions. In general, the calculated results, obtained by a fitting procedure described in the Appendix, are found to be in a good agreement with the empirical data.

The results of the comprehensive analysis suggest a complex phase structure in these isotopes, involving two configurations. The normal A configuration remains spherical in all isotopes considered. The intruder B configuration undergoes a spherical to axially deformed U(5)-SU(3) QPT within the boson core, with a critical point near $A \approx 100$. In parallel to the gradual shape evolution within configuration B, the two configurations cross near neutron number 60, and the ground state changes from configuration A to configuration B. The two configurations are weakly mixed and retain their purity before and after the crossing, thus demonstrating IQPTs in odd-mass nuclei.

The new IBFM-CM framework can motivate further work in any medium-heavy odd-mass region with mixed configurations, such as $Z \approx 40, 50, 82$ and $N \approx 60, 66, 104$, respectively, with many nuclei to be explored. The current results obtained for the Nb isotopes motivate further experiments of non-yrast spectroscopy in such nuclei, as well as set the path for new investigations on multiple QPTs and coexistence in other Bose-Fermi systems.

ACKNOWLEDGMENTS

The author would like to acknowledge support by the Israel Academy of Sciences of a Postdoctoral Fellowship Program in Nuclear Physics. The author would like to thank F. Iachello (Yale University) and A. Leviatan (Hebrew University) for their enlightening comments, discussions and encouragement, and to P. Van Isacker for providing his IBFM code, which served as a basis for the IBFM-CM computer program.

APPENDIX: SINGLE-PARTICLE ENERGIES AND BCS PROCEDURE

A BCS calculation is done by iterating over the equations for the single-quasiparticle energies (ϵ_j) and occupation probabilities (v_j^2), as one varies the Fermi energy λ_F, until an equality between the particle number (N_p) and the number of valence particles is obtained:

$$\epsilon_j = \sqrt{(E_j - \lambda_F)^2 + \Delta_F}, \tag{A1}$$

$$v_j^2 = \frac{1}{2}\left(1 - \frac{E_j - \lambda_F}{\epsilon_j}\right), \tag{A2}$$

$$N_p = \sum_j (2j+1) v_j^2. \tag{A3}$$

In Eq. (A1), j are the different shell orbits, E_j are the experimental single-particle energies, and Δ_F is the pairing gap. In this work, for $_{41}$Nb the BCS procedure is employed with 13 valence particle in the $Z = 28$–50 shell with the $\pi(1f_{5/2}), \pi(2p_{1/2}), \pi(2p_{3/2}), \pi(1g_{9/2})$ orbits. The same

single-particle energies and pairing gap for both configurations A and B are chosen. It might be possible to choose a different set of single-particle energies for the intruder configuration—however, this is not done so for simplicity. The experimental single-particle energies are taken from Table XI of [83] and Δ_F is taken to be 1.5 MeV, consistent with the values of the empirical proton pairing gaps (see Eq. (2.93) of [84]) for $^{91-97}$Nb. The resulting single-quasiparticle energies (ϵ_j) and occupation probabilities (v_j^2) are shown in Table I for the different orbits and single-particle energies (E_j). Taking the derived ϵ_j and v_j^2, the parameters of the boson-fermion interaction (12a) can be determined from the microscopic theory of the IBFM to be

$$A_j^{(i)} = -\sqrt{5(2j+1)}A_0^{(i)}, \tag{A4}$$

$$\Gamma_{jj'}^{(i)} = \sqrt{5}\gamma_{jj'}\Gamma_0^{(i)}, \tag{A5}$$

$$\Lambda_{jj'}^{(i)j''} = -2\sqrt{\frac{5}{2j''+1}}\beta_{jj''}\beta_{j'j''}\Lambda_0^{(i)}, \tag{A6}$$

where i = A,B for the different configurations and

$$\gamma_{jj'} = (u_j u_{j'} - v_j v_{j'})Q_{jj'}, \tag{A7}$$

$$\beta_{jj'} = (u_j v_{j'} + v_j u_{j'})Q_{jj'}, \tag{A8}$$

$$Q_{jj'} = \langle j||Y^{(2)}||j'\rangle, \tag{A9}$$

where the occupation probability u_j satisfies $u_j^2 = 1 - v_j^2$.

The strengths ($A_0^{(i)}$, $\Gamma_0^{(i)}$, $\Lambda_0^{(i)}$) are obtained by a fit, and can be separated to positive- and negative-parity states and to the different configurations. In this work, for simplicity, the same values for the different configurations are assumed. They are listed in Table II, where the monopole term (A_0) vanishes for neutron number 52–56 and corrects the quasiparticle energies at neutron number 58–62. The quadrupole term (Γ_0) is constant for the entire chain. The exchange term (Λ_0) increases towards the neutron midshell [18]. Altogether, the values of the parameters are either constant for the entire chain or segments of it and vary smoothly. Interestingly, these values are very similar to those of the $_{63}$Eu isotopes [85] in a single-shell configuration and a single-j calculation with $v^2 = 0.3$, which have an approximately constant value of $\Gamma_0 \approx 1$ and $A_0 = -0.4$ and an increasing value of Λ_0 from ≈ 1.6 in the spherical region to ≈ 3.8 in the deformed one. For the boson-fermion mixing term, $\hat{W}_{\rm bf}$ of Eq. (10), the value of $\omega_j = 0$ is chosen, since for equal ω_j it coincides with the $\hat{W}_{\rm b}$ term of Eq. (5).

For $\hat{T}_{\rm b}(M1)$ of Eq. (17), the values $g^{(\rm A)} = -0.21\,\mu_N$, $-0.42\,\mu_N$ are used for neutron number 52–54 and zero otherwise, $g^{(\rm B)} = (Z/A)\mu_N$ and $\tilde{g}^{(\rm A)} = \tilde{g}^{(\rm B)} = 0$ ($-0.017\,\mu_N$) for 52–56 (58–62), where Z and A correspond to the even-even Zr boson core. For $\hat{T}_{\rm f}(M1)$ the value $g_\ell = 1\mu_N$ is used and a quenching of 20.835%, which results in a value of $g_s = 4.4219\,\mu_N$.

For $\hat{T}_{\rm b}(E2)$ of Eq. (14), the same parameters ($e^{(\rm A)}$, $e^{(\rm B)}$, χ) are adopted for the core Zr isotopes [12], with a slight modification of $e^{(\rm A)} = 2.45$, $1.3375\ \sqrt{\rm W.u.}$ for neutron numbers 52–54 and $e^{(B)} = 2.0325\ \sqrt{\rm W.u.}$ for 62. The fermion effective charge in $\hat{T}_{\rm f}(E2)$ is $e_f = -2.361\sqrt{\rm W.u.}$, determined from a fit to the ground state quadrupole moment of ^{93}Nb.

[1] R. Gilmore and D. H. Feng, Phys. Lett. B **76**, 26 (1978).
[2] R. Gilmore, J. Math. Phys. **20**, 891 (1979).
[3] P. Cejnar, J. Jolie, and R. F. Casten, Rev. Mod. Phys. **82**, 2155 (2010).
[4] *Understanding Quantum Phase Transitions*, edited by L. D. Carr (CRC, Boca Raton, FL, 2010).
[5] A. E. L. Dieperink, O. Scholten, and F. Iachello, Phys. Rev. Lett. **44**, 1747 (1980).
[6] F. Iachello, Nuovo Cimento **34**, 617 (2011).
[7] K. Heyde and J. L. Wood, Rev. Mod. Phys. **83**, 1467 (2011).
[8] A. Frank, P. Van Isacker, and F. Iachello, Phys. Rev. C **73**, 061302(R) (2006).
[9] P. Federman and S. Pittel, Phys. Rev. C **20**, 820 (1979).
[10] N. Gavrielov, A. Leviatan, and F. Iachello, Phys. Rev. C **99**, 064324 (2019).
[11] N. Gavrielov, A. Leviatan, and F. Iachello, Phys. Scr. **95**, 024001 (2020).
[12] N. Gavrielov, A. Leviatan, and F. Iachello, Phys. Rev. C **105**, 014305 (2022).
[13] R. F. Casten, Prog. Part. Nucl. Phys. **62**, 183 (2009).
[14] L. Fortunato, Prog. Part. Nucl. Phys. **121**, 103891 (2021).
[15] E. Caurier, G. Martínez-Pinedo, F. Nowack, A. Poves, and A. P. Zuker, Rev. Mod. Phys. **77**, 427 (2005).
[16] B. Bally, B. Avez, M. Bender, and P.-H. Heenen, Phys. Rev. Lett. **113**, 162501 (2014).
[17] O. Scholten and N. Blasi, Nucl. Phys. A **380**, 509 (1982).
[18] F. Iachello and P. Van Isacker, *The Interacting Boson-Fermion Model* (Cambridge University Press, Cambridge, 1991).
[19] J. Jolie, S. Heinze, P. Van Isacker, and R. F. Casten, Phys. Rev. C **70**, 011305(R) (2004).
[20] C. E. Alonso, J. M. Arias, L. Fortunato, and A. Vitturi, Phys. Rev. C **72**, 061302(R) (2005).
[21] C. E. Alonso, J. M. Arias, and A. Vitturi, Phys. Rev. C **75**, 064316 (2007).
[22] C. E. Alonso, J. M. Arias, L. Fortunato, and A. Vitturi, Phys. Rev. C **79**, 014306 (2009).
[23] M. Böyükata, P. Van Isacker, and Ä. Uluer, J. Phys. G: Nucl. Part. Phys. **37**, 105102 (2010).
[24] D. Petrellis, A. Leviatan, and F. Iachello, Ann. Phys. (NY) **326**, 926 (2011).
[25] F. Iachello, A. Leviatan, and D. Petrellis, Phys. Lett. B **705**, 379 (2011).
[26] M. Böyükata, C. E. Alonso, J. M. Arias, L. Fortunato, and A. Vitturi, Symmetry (Basel). **13**, 215 (2021).
[27] K. Nomura, T. Otsuka, and P. Van Isacker, J. Phys. G **43**, 024008 (2016).
[28] K. Nomura, T. Nikšić, and D. Vretenar, Phys. Rev. C **93**, 054305 (2016).
[29] K. Nomura, T. Nikšić, and D. Vretenar, Phys. Rev. C **102**, 034315 (2020).
[30] S. Quan, Z. P. Li, D. Vretenar, and J. Meng, Phys. Rev. C **97**, 031301(R) (2018).

[31] S. Brant, V. Paar, and A. Wolf, Phys. Rev. C **58**, 1349 (1998).
[32] R. Rodriguez-Guzman, P. Sarriguren, and L. M. Robledo, Phys. Rev. C **83**, 044307 (2011).
[33] P. Spagnoletti, G. Simpson, S. Kisyov, D. Bucurescu, J.-M. Régis, N. Saed-Samii, A. Blanc, M. Jentschel, U. Köster, P. Mutti, T. Soldner, G. de France, C. A. Ur, W. Urban, A. M. Bruce, C. Bernards, F. Drouet, L. M. Fraile, L. P. Gaffney, D. G. Ghiță *et al.*, Phys. Rev. C **100**, 014311 (2019).
[34] P. E. Garrett, Phys. Rev. Lett. **127**, 169201 (2021).
[35] E. Cheifetz, R. C. Jared, S. G. Thompson, and J. B. Wilhelmy, Phys. Rev. Lett. **25**, 38 (1970).
[36] K. Heyde, P. Van Isacker, R. F. Casten, and J. L. Wood, Phys. Lett. B **155**, 303 (1985).
[37] K. Heyde, J. Jolie, J. Moreau, J. Ryckebusch, M. Waroquier, P. V. Duppen, M. Huyse, and J. L. Wood, Nucl. Phys. A **466**, 189 (1987).
[38] P. Federman and S. Pittel, Phys. Lett. B **69**, 385 (1977).
[39] P. Federman, S. Pittel, and R. Campos, Phys. Lett. B **82**, 9 (1979).
[40] P. Federman, S. Pittel, and A. Etchegoyen, Phys. Lett. B **140**, 269 (1984).
[41] H. Mach, E. K. Warburton, W. Krips, R. L. Gill, and M. Moszyński, Phys. Rev. C **42**, 568 (1990).
[42] T. Togashi, Y. Tsunoda, T. Otsuka, and N. Shimizu, Phys. Rev. Lett. **117**, 172502 (2016).
[43] P. E. Garrett, M. Zielińska, and E. Clément, Prog. Part. Nucl. Phys. **124**, 103931 (2022).
[44] G. Lhersonneau, H. Gabelmann, M. Liang, B. Pfeiffer, K.-L. Kratz, H. Ohm (ISOLDE Collaboration), Phys. Rev. C **51**, 1211 (1995).
[45] G. Lhersonneau, B. Pfeiffer, J. R. Persson, J. Suhonen, J. Toivanen, P. Campbell, P. Dendooven, A. Honkanen, M. Huhta, P. M. Jones, R. Julin, S. Juutinen, M. Oinonen, H. Penttilä, K. Peräjärvi, A. Savelius, W. Jicheng, J. C. Wang, and J. Äystö, Z. Phys. A **358**, 317 (1997).
[46] A. Esmaylzadeh, J.-M. Régis, Y. H. Kim, U. Köster, J. Jolie, V. Karayonchev, L. Knafla, K. Nomura, L. M. Robledo, and R. Rodriguez-Guzman, Phys. Rev. C **100**, 064309 (2019).
[47] D. Gloeckner, Nucl. Phys. A **253**, 301 (1975).
[48] D. Bucurescu, Z. Podolyàk, C. Rusu, G. de Angelis, Y. H. Zhang, G. Căta-Danil, I. Căta-Danil, M. Ivaşcu, N. Mărginean, R. Mărginean, L. C. Mihăilescu, G. A. Suliman, P. H. Regan, W. Gelletly, S. D. Langdown, J. J. Valiente-Dobón, D. Bazzacco, S. Lunardi, C. A. Ur, M. Axiotis *et al.*, Phys. Rev. C **71**, 034315 (2005).
[49] J. N. Orce, J. D. Holt, A. Linnemann, C. J. McKay, S. R. Lesher, C. Fransen, J. W. Holt, A. Kumar, N. Warr, V. Werner, J. Jolie, T. T. S. Kuo, M. T. McEllistrem, N. Pietralla, and S. W. Yates, Phys. Rev. Lett. **97**, 062504 (2006).
[50] J. N. Orce, J. D. Holt, A. Linnemann, C. J. McKay, C. Fransen, J. Jolie, T. T. S. Kuo, S. R. Lesher, M. T. McEllistrem, N. Pietralla, N. Warr, V. Werner, and S. W. Yates, Phys. Rev. C **82**, 044317 (2010).
[51] S. Brant, K. Sistemich, V. Paar, and G. Lhersonneau, Z. Physik A **330**, 365 (1988).
[52] G. Lhersonneau, B. Pfeiffer, K. L. Kratz, H. Ohm, K. Sistemich, S. Brant, and V. Paar, Z. Phys. A **337**, 149 (1990).
[53] G. Lhersonneau, J. Suhonen, P. Dendooven, A. Honkanen, M. Huhta, P. Jones, R. Julin, S. Juutinen, M. Oinonen, H. Penttilä, J. R. Persson, K. Peräjärvi, A. Savelius, J. C. Wang, J. Äystö, S. Brant, V. Paar, and D. Vretenar, Phys. Rev. C **57**, 2974 (1998).
[54] F. Boulay, G. S. Simpson, Y. Ichikawa, S. Kisyov, D. Bucurescu, A. Takamine, D. S. Ahn, K. Asahi, H. Baba, D. L. Balabanski, T. Egami, T. Fujita, N. Fukuda, C. Funayama, T. Furukawa, G. Georgiev, A. Gladkov, M. Hass, K. Imamura, N. Inabe *et al.*, Phys. Rev. Lett. **124**, 112501 (2020).
[55] K. Sieja, F. Nowacki, K. Langanke, and G. Martínez-Pinedo, Phys. Rev. C **79**, 064310 (2009).
[56] K. Sieja, Universe **8**, 23 (2021).
[57] N. Gavrielov, A. Leviatan, and F. Iachello, Phys. Rev. C **106**, L051304 (2022).
[58] F. Iachello and I. Talmi, Rev. Mod. Phys. **59**, 339 (1987).
[59] P. D. Duval and B. R. Barrett, Phys. Lett. B **100**, 223 (1981).
[60] P. D. Duval and B. R. Barrett, Nucl. Phys. A **376**, 213 (1982).
[61] M. Sambataro and G. Molnár, Nucl. Phys. A **376**, 201 (1982).
[62] J. E. García-Ramos and K. Heyde, Phys. Rev. C **89**, 014306 (2014).
[63] J. E. García-Ramos, K. Heyde, L. M. Robledo, and R. Rodriguez-Guzman, Phys. Rev. C **89**, 034313 (2014).
[64] J. E. García-Ramos and K. Heyde, Phys. Rev. C **92**, 034309 (2015).
[65] K. Nomura, R. Rodriguez-Guzman, and L. M. Robledo, Phys. Rev. C **94**, 044314 (2016).
[66] A. Leviatan, N. Gavrielov, J. E. García-Ramos, and P. Van Isacker, Phys. Rev. C **98**, 031302(R) (2018).
[67] E. Maya-Barbecho and J. E. García-Ramos, Phys. Rev. C **105**, 034341 (2022).
[68] R. D. Lawson and J. L. Uretsky, Phys. Rev. **108**, 1300 (1957).
[69] A. Bohr and B. R. Mottelson, *Nuclear Structure*, Vol. 2 (World Scientific, Singapore, 1998).
[70] C. M. Baglin, Nucl. Data Sheets **112**, 1163 (2011).
[71] S. Basu, G. Mukherjee, and A. Sonzogni, Nucl. Data Sheets **111**, 2555 (2010).
[72] N. Nica, Nucl. Data Sheets **111**, 525 (2010).
[73] E. Browne and J. Tuli, Nucl. Data Sheets **145**, 25 (2017).
[74] I. J. van Heerden, W. R. McMurray, and R. Saayman, Z. Phys. **260**, 9 (1973).
[75] Evaluated Nuclear Structure Data File (ENSDF), https://www.nndc.bnl.gov/ensdf.
[76] T. W. Hagen, A. Görgen, W. Korten, L. Grente, M.-D. Salsac, F. Farget, I. Ragnarsson, T. Braunroth, B. Bruyneel, I. Celikovic, E. Clément, G. de France, O. Delaune, A. Dewald, A. Dijon, M. Hackstein, B. Jacquot, J. Litzinger, J. Ljungvall, C. Louchart *et al.*, Phys. Rev. C **95**, 034302 (2017).
[77] D. De Frenne, Nucl. Data Sheets **110**, 2081 (2009).
[78] M. Hotchkis, J. Durell, J. Fitzgerald, A. Mowbray, W. Phillips, I. Ahmad, M. P. Carpenter, R. V. F. Janssens, T. Khoo, E. Moore, L. Morss, P. Benet, and D. Ye, Nucl. Phys. A **530**, 111 (1991).
[79] Y.-A. Luo, J. O. Rasmussen, I. Stefanescu, A. Gelberg, J. H. Hamilton, A. V. Ramayya, J. K. Hwang, S. J. Zhu, P. M. Gore, D. Fong, E. F. Jones, S. C. Wu, I. Y. Lee, T. N. Ginter, W. C. Ma, G. M. Ter-Akopian, A. V. Daniel, M. A. Stoyer, and R. Donangelo, J. Phys. G: Nucl. Part. Phys. **31**, 1303 (2005).
[80] C. M. Baglin, Nucl. Data Sheets **114**, 1293 (2013).
[81] W. Huang, G. Audi, M. Wang, F. G. Kondev, S. Naimi, and X. Xu, Chin. Phys. C **41**, 030002 (2017).

[82] B. Cheal, K. Baczynska, J. Billowes, P. Campbell, F. C. Charlwood, T. Eronen, D. H. Forest, A. Jokinen, T. Kessler, I. D. Moore, M. Reponen, S. Rothe, M. Rüffer, A. Saastamoinen, G. Tungate, and J. Äystö, Phys. Rev. Lett. **102**, 222501 (2009).

[83] J. Barea and F. Iachello, Phys. Rev. C **79**, 044301 (2009).

[84] A. Bohr and B. R. Mottelson, *Nuclear Structure*, Vol. 1 (World Scientific, Singapore, 1998).

[85] O. Scholten, The interacting boson approximation model and applications, Ph.D. thesis, University of Groningen, 1980.